EFFECT OF MECHANICAL ABRASION ON OIL/WATER CONTACT ANGLE IN METALS

by

Simin Salam Tabrizi

A Thesis Submitted in

Partial Fulfillment of the

Requirements for the Degree of

Master of Science

in Engineering

at

The University of Wisconsin-Milwaukee

August 2012

ABSTRACT

EFFECT OF MECHANICAL ABRASION ON OIL/WATER CONTACT ANGLE IN METALS

by

Simin Salam Tabrizi

The University of Wisconsin-Milwaukee
Under the Supervision of Professor Pradeep Rohatgi

In this study the oil/water angle for brass, aluminum, hastelloy and 316 stainless steel was experimentally studied as a function of surface roughness. Samples were mechanically abraded by sandpaper in the way that all the scratches were parallel. Surface roughness was measured by profilometer, Nano-Indenter, and Atomic Force Microscope (AFM). The relationship between sandpaper particle size and surface roughness for all four metals was established. The highest surface roughness obtained for steel 316 ground by 180 grit sandpaper (1.23μm) and the smoothest surfaces were achieved for brass and aluminum after grinding with alumina (0.03 μm).Then oil/water contact angles were measured by Rame Hart Goniometer. Results showed that contact angle on brass increases with increasing the surface roughness from 88˚ on smooth brass to 128˚ on 60 grit ground sample. Smooth hastelloy had a contact angle (97˚) lower than rough sample (110˚). Contact angle of oil in water on fine polished aluminium decrease from 122˚ to 108˚ on 1200 grit and then increases with increasing the surface roughness to 125˚ on 60 grit. Contact angle of oil on steel increases from 83˚ on fine polished to 97˚ on 320 grit and then decreases with increasing the surface roughness and reach 77˚ on 60 grit.

A model is presented for calculating R_f and f_{so} when samples are ground parallel with sandpaper of known particle size and surface roughness and they have been used to calculate contact angle for both Wenzel and Cassie-Baxter types of contacts.

Predicted values were compared with experimentally measured values. Results showed that aluminum followed Wenzel model, brass and hastelloy followed Cassie-Baxter model and stainless steel 316 exhibited a transition from Wenzel to Cassie-Baxter with a change in R_f.

TABLE OF CONTENTS

LIST OF FIGURES

LIST OF TABLES

ACKNOWLEDGMENTS

I am grateful to my advisor. Professor P. Rohatgi for his wisdom, support and guidance throughout my work in Composites and Advanced Materials Manufacture. I would like to thank the member of my defence committee, Professors Ben Church and Konstantin Sobolev.

Dr. JB Ferguson, and Dr. Ben Schultz have my sincere gratitude for their assistance, support and guidance.

I extend special thanks to Dr. M. Nosonovsky. I also thank Dr. Steven Hardcastle from the Advance Analysis Facility of University of Wisconsin.

I dedicate this work to my parents Asghar and Maryam Salam Tabrizi, to my family for whom my love and gratitude hold no bound.

Chapter 1

Introduction

1. Introduction

In this section to ease the understanding the concepts of some basic terms and definitions are presented.

1.1 Surface Energy

Surface energy, γ, represents the disruption of intermolecular bonds that occurs when a surface is created. Molecules on the surface have higher energy than ones in the bulk due to their broken bonds [5].

Surface energy can be defined in term of Gibbs free energy:

$$\partial G = -S\partial T + V\partial P + \gamma\partial A$$

$$\gamma = \left(\frac{\partial G}{\partial A}\right)_{T,P}$$

1.2 Surface Roughness

Variation in height of the surface from reference plane is called surface roughness. It could be measured by a single line or a several parallel lines (surface maps). There are different standards for surface roughness, which are: [6]

a) $\boldsymbol{R_a}$, CLA, or AA is known as average roughness. R_a is a linear measurement and measures the average value of departure of profile from center line.

b) $\boldsymbol{R_q}$ is known as square root, R_s, or RMS is an average of root mean square value.

c) ***Rt***, which is known as R_{max} or R_y, is the maximum peak-to-valley height.

d) $\boldsymbol{R_p}$ is maximum peak-to-mean height.

e) $\boldsymbol{R_v}$ is maximum valley depth (mean-to-lowest valley height).

f) $\boldsymbol{R_z}$ is average peak-to-valley height.

g) $\boldsymbol{R_{pm}}$ is average peak-to-mean height.

h) $\boldsymbol{R_f}$ is surface roughness factor, rate of actual to projected area.

1.3 Contact angle

When a droplet is placed on the surface of a solid, three boundaries will form; i.e. solid-water, water- air, and solid-air. The angle θ between water droplet and solid is called contact angle as shown in Fig.1.1 [7].

When a liquid droplet contacts with a smooth solid surface under the angle θ (Fig. 1), the net energy change for propagation of the liquid front for a small distance dx is equal to$(\gamma_{SL} - \gamma_{SG} + \gamma_{LG}\cos\theta)dx$.

Thus, for the liquid front being at equilibrium, the Young equation can be written as [8]:

$$\cos\theta = \frac{\gamma_{SG}-\gamma_{SL}}{\gamma_{LG}} \qquad (1.1)$$

where γ_{SL}, γ_{SG} and γ_{LG} are solid-liquid, solid-gas and liquid-gas interfacial energies, respectively.

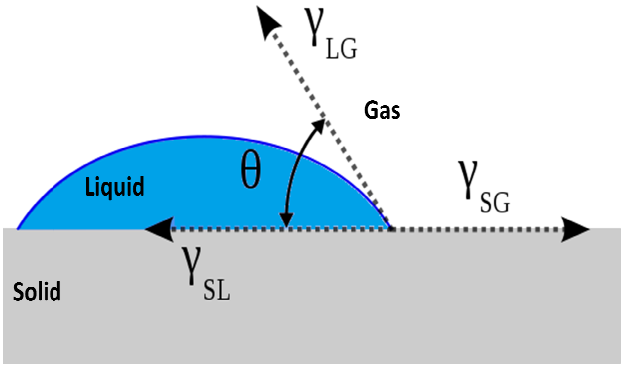

Figure 1.1 Contact angle of water.

If ———=1, it means θ=0˚, so surface would be completely wetted by liquid. If ——— , then θ=180˚and solid would repealed the liquid.

Ponter at el. [9] modified the Young Equation to:

cosθ= cos - — – (1.2)

cos = ——— (1.3)

Where σ is the line tension, R is the radius of the three-phase contact circle, θ is the contact angle of a finite contact radius R, and is the contact angle of infinitely large drop, i.e. , corresponding to R= .

Besides materials properties, roughness, surface preparation procedure, and cleanliness could affect the contact angle [10]. Li et al [11] presented a model that indicates that increasing the contact angle with increasing the droplet size is not only due to negative line tension, it could be the effect of corrugation of the three-phase line caused by the

imperfection of the solid surface. Pierre at el [12] showed that drop volume has a significant effect on contact angle. In this study a droplet size of between 10-20 mL was used since variation in this range did not show a change in contact angle with 304 stainless steel.

1.4 Hydrophobic- hydrophilic/ Oleophobic- Oleophilic Surfaces

When a surface repels liquid, it is called hydrophobic or oleophobic, which means that the contact angle of oil and solid is greater than 90°, when the contact angle is below 90° it is called hydrophilic or oleophilic [13].

1.5 Models for Wetting of Rough Surfaces

Two regimes for wetting of the rough surfaces have been developed.

1. Homogeneous regime with a two-phase solid–water interface (Wenzel) [14]

2. Non-homogeneous or composite regime with a three-phase solid– water–air interface (Cassie-Baxter) [15]

1.5.1 Wenzel Model

Wenzel [14] used energy balance to drive an equation for water contact angle on fabrics. When a water droplet is placed on a surface, two new interfaces will form, water/substrate and water/air. Water/substrate area will be equal to disappeared substrate-air area. The three interfaces (water/air, water/solid, and solid/air) have different surface energies. If the wetted area has lower surface energy, water droplet will trend to spread on its surface this is called “wetting” which involves energy release. In a constant condition higher water/solid contact area results in more interest to spread the water droplet than smooth surfaces. If solid/air has highest surface energy among all three

surface interfaces, water droplet will be repelled and will form a near spherical shape. In this case also increasing the solid/water area increases the repelling. Wenzel defines a roughness factor, R_f , by Eq.1.4.

$$R_f = \frac{actual\ surface\ area}{Projected\ surface\ are} \qquad (1.4)$$

For smooth surfaces, surface roughness is equal to one. Wenzel used force balance to obtain Eq. 1.5. [14]

$$\cos \theta_w = R_f \cos \theta_0 \qquad (1.5)$$

where θ_0 is contact angle of smooth surface and θ_w is predicted contact angle by Wenzel.

Nosonovsky et al. [1] has made the point that according to Wenzel model, if $\theta<90^\circ$ increasing the surface roughness decreases contact angle and if $\theta>90^\circ$ increasing the surface roughness increases contact angle. Fig. 1.2 depicts the effect of roughness on contact angle. In this research it would be shown that aluminum will have Wenzel behavior and its smooth surface contact angle is more than 90˚. Experiment results showed that contact angle drops with increasing R_f and then increases.

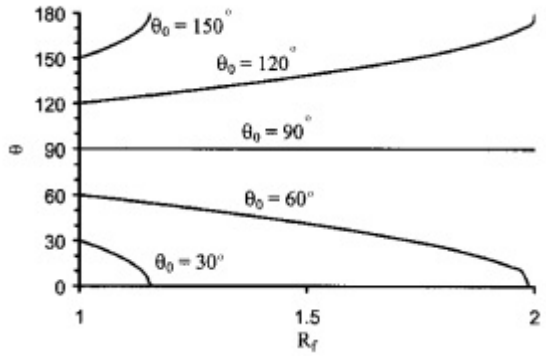

Figure 1.2 Contact angle for rough surface (θ) as a function of the roughness factor (R_f) for various contact angles of the smooth surface (θ_0) **[1]**.

1.5.2 Cassie-Baxter Model

Fig. 1.3 shows the schematic of placing a droplet on a substrate. Fig 1.3.a shows a droplet on a flat surface while Fig 1.3.b and c show a droplet on rough surfaces. In this figure Wenzel and Cassie-Baxter regimes are demonstrated.

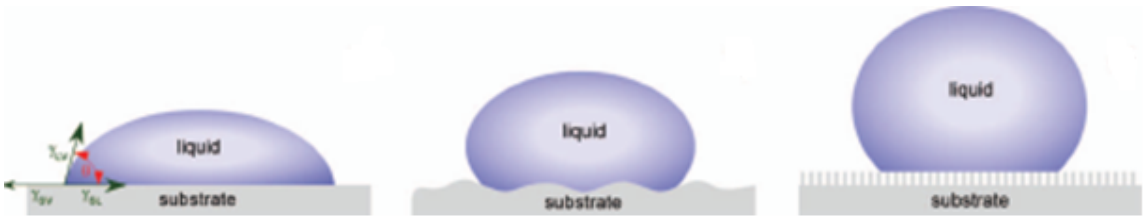

(a) (b) (c)

Figure 1.3 Schematic of droplet on a) flat surface, b) and c) rough surfaces. Depending on the roughness it could be b) Wenzel or c) Cassie-Baxter regime. **[1]**

Cassie and Baxter [15] developed a model for porous materials. They assumed that there is no hydrostatic pressure on the system. They found an equation for net energy, E,:

$$E = f_1 (\gamma_{LS} - \gamma_{SA}) + f_2 \gamma_{LA} \qquad (1.6)$$

where, f_1 is the total area of solid-liquid interface, f_2 is the total area of liquid-air, γ_{LS} is liquid-solid surface energy, γ_{SA} is solid-air surface energy, and γ_{LA} is liquid-air surface energy. Also, according to the Young equation:

$$\cos\theta_A = (\gamma_{SA} - \gamma_{LS}) / \gamma_{LA} \qquad (1.7)$$

Here, θ_A is advancing contact angle for solid-liquid interface. Therefore, Eq. 1.2 will change to:

$$\cos\theta_{CB} = \frac{-E}{\gamma_{LA}} = f_1 \cos\theta_A - f_2 \qquad (1.8)$$

where, θ_{CB} is an apparent angle. Nosonovsky et al [1] have used modified Cassie-Baxter equation for oil contact angle in water:

$$\cos\theta_{CB} = f_{SL}(\cos\theta_0 + 1) - 1 \qquad (1.9)$$

$$\cos\theta_{CB} = f_{SL}(R_f \cos\theta_0 + 1) - 1 \qquad (1.10)$$

or,

$$\cos\theta_{CB} = f_{SO}\cos\theta_{SO} + f_{WO}\cos\theta_{WO} \qquad (1.11)$$

Here, f_{SL} and f_{LG} are solid-liquid and liquid-gas interface area, respectively. "O" refers to *oil*, "W" refers to *water* and "S" refers to *solid*. The effect of surface roughness on contact angle is shown in Fig. 1.4. This model shows that for hydrophilic and hydrophobic surfaces, the contact angle increases with an increase in f_{LG} both for smooth and rough surfaces. [2]

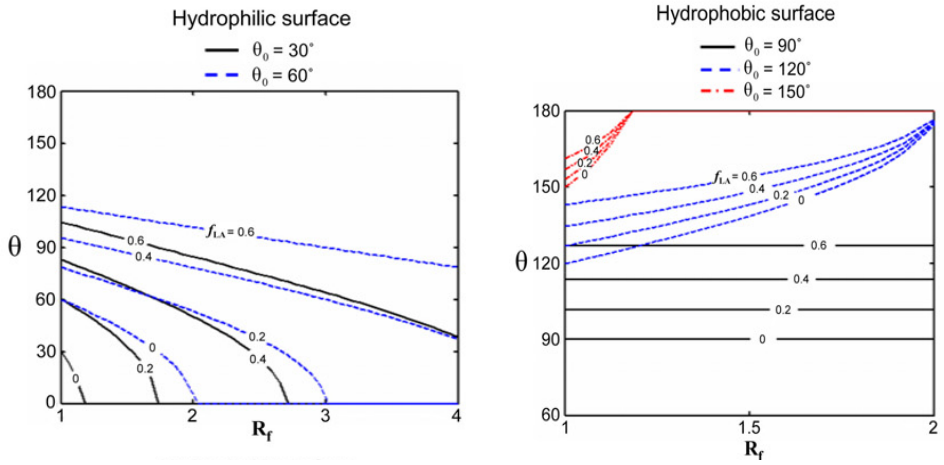

Figure 1.4 Effect of surface roughness of contact angle **[2]**.

In the Cassie-Baxter regime, contact angle depends on the proportions of the interfacial areas of the three materials, f_{SO} and f_{WO}. Gao and McCarthy [16] have pointed out that the contact angle behavior is determined by interactions of the liquid and the solid at the three-phase contact line rather than over the entire interfacial area. Their experiments show that for surfaces in which the structure under the drop is different from the structure at the interfacial line, the Cassie-Baxter equation is not valid. However, McHale [17] points out that Eq. 2.8 will be valid for a drop with a size considerably larger than the features of a uniform surface, because in this case the structure under the entire drop contact area can be considered the same as that encountered at the interface. In the case of the uniform surface, the fraction of the length of the solid/oil interface, $L_{SO}/(L_{SO}+L_{WO})$, can be determined from solid/oil contact area, A_{SO}, and the total contact area, $A_{SO}+A_{WO}$, according to Equation (1.12).

$$f_{SO}=\frac{L_{SO}}{L_{SO}+L_{WO}}\cong\frac{A_{SO}}{A_{SO}+A_{WO}} \tag{1.12}$$

The fraction of oil/water can be determined in the same way, but because$f_{SO}+f_{WO}=1$, it can also be defined in terms of f_{SO} according to Eq. (1.13).

$$f_{WO}=\frac{L_{WO}}{L_{SO}+L_{WO}}\cong\frac{A_{WO}}{A_{SO}+A_{WO}}=1-f_{SO} \tag{1.13}$$

Because roughness along the solid/oil interface can influence the contact angle, it is necessary to take it into consideration. However, it should be noted that the roughness factor in this case, $R_{f_{CB}}$, applies only to the solid/oil regions rather than to the entire contact region as in the Wenzel model. Lastly, oil and water are immiscible and the contact angle between them can be considered to be 180^o. Thus Eq. 1.11 can be recast taking all of the above into consideration, resulting in Equation (1.14).

$$\cos\theta_{CB}=f_{SO}R_{f_{CB}}\cos\theta_o+(1-f_{SO})\cos 180^o=f_{SO}\left(R_{f_{CB}}\cos\theta_o+1\right)-1 \tag{1.14}$$

According to Young eq, a low surface tension fluid such as oil to have a contact angle higher than 90˚, γ_{SW} must be lower than those of the other surfaces. Therefore, Wenzel model will be preferred [18].

Later, Shafrin et al [19] claimed that only atoms on the surface are affecting the contact angle and atoms more than a few atom diameters below the surface have no influence on wetting behavior of the substrate.

1.5.3 Wenzel to Cassie-Baxter Transition

Wetting transitions have been intensively studied recently due to their importance for the superhydrophobicity and oleophobicity [20, 21, 13]. Fig. 1.5 shows the prediction of Wenzel and Cassie-Baxter [3]. Here φ_s is solid fraction area, and θ^* is apparent contact angle. Quere et al. [3] showed that if material is highly hydrophobic air pockets will form between liquid and substrate. If the energy required to replace a dry surface by a wet one is not too high air pockets cannot develop. Increasing the hydrophobicity of the solid is indicated in Fig. 1.5 with full lines. Fig. 1.5 also implies that for moderate roughness and hydrophobicity, angles under Wenzel type of contact are expected to be smaller than under Cassie-Baxter type of contact. When contact angle is higher than 90◦ and lower than θ_c, Wenzel type of contact is expected. When air is trapped below the drop Cassie-Baxter model will be followed ($\theta > \theta c$). The respective slopes of the lines are r and φ_s. This metastable situation is shown by the dotted line in this Figure.

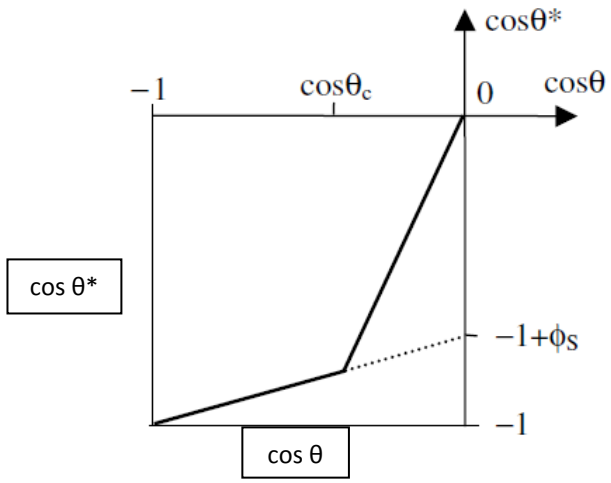

Figure 1.5 The different models of super-hydrophobicity **[3]**.

Figure 1.6 shows that a metastable Cassie-Baxter droplet can go to stable Wenzel regime by applying small pressure (Fig 1.6.c) or evaporation of liquid (Fig 1.6.d). The amount of liquid in droplet is a main parameter to determine the regime (Fig 1.6.e) [4].

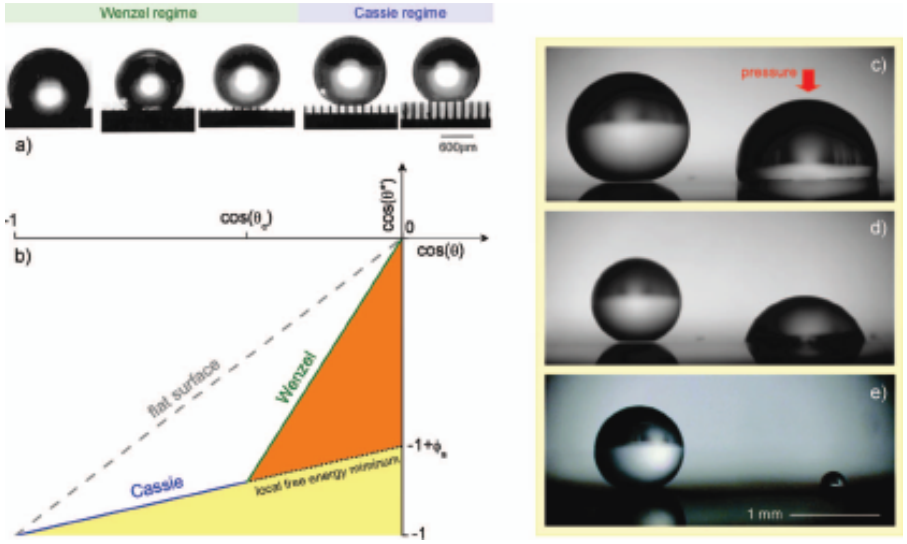

Figure 1.6 (a) Shapes of water droplets spreading on pillar structures with varying roughness factor (R). (b) A diagram depicting the transition between the Cassie and Wenzel wetting regimes. (c) and (e) Water droplet deposited on a surface in Cassie (left drop) and Wenzel right drop) regimes, (d) evaporating some liquid, and (e) adjusting the volume of the drop **[4]**

There is a significant change in measured contact angle of small and large drop. Contact angle may decreases with reducing the drop size [22, 23]. Savoy at el. showed that topology and droplet size have a significant effect on transition of Cassie-Baxter to Wenzel model [18].

The design of surface topology and chemistry to promote desired wetting behavior is of interest for applications such as microfluidic systems, anti-biofouling, biosensing, heat exchange, and self-cleaning surfaces [24]. Water has a high surface tension and polarity which make it easy to achieve superhydrophobic surfaces while obtaining an oleophobic surface is not that easy due to low surface tension of oil.

Chapter 2

Experimental methods and materials

2. Experiment

2.1 Materials:

In this study stainless steel 316 (SS 316), brass C84400, commercially pure aluminium, and hastelloy C22 were used to test accuracy of the models to be presented in chapter 4. The compositions of metals are given in Table 2.1, 2.2, and 2.3.

Table 2.1Chemical composition of stainless steel 316 and 304.

Metal	% wt								
	C	Cr	Ni	Mo	Mn	Si	P	S	Fe
SS 316	<0.03	16-18.5	10-14	2-3	<2	<1	<0.045	<0.03	Balanced

Table 2.2Chemical composition of brass C84400.

Metal	% wt										
	Sb	Cu	Fe	Pb	Ni	P	Si	S	Al	Sn	Zn
Brass C84400	<0.25	78-82	<0.40	6-8	<1	<0.02	<0.005	<0.08	<0.005	2.3-3.5	7-10

Table 2.3Chemical composition of hastelloy C22.

Element	Co	Cr	Mo	W	Fe	Si	Mn	C	Ni	V
%wt	<2.5	22	13	3	3	<0.08	<0.5	<0.01	Balance	<0.35

2.2 Methods

Selected approach to roughen the metal surface in the present research was mechanical abrasion.

Mechanical abrasion was performed using Buehler polishing machine (Buehler MetaServ®3000) 60 ,180, 240, 320,400, 600 ,800 and 1200 grit Buehler SiC sandpapers with particle size of 269, 82 , 52.2, 35, 21.8, 15.3, 12.6, and 8.4µm ,respectively.

Polishing and grinding has been done at 250 rpm in the way that all scratches were aligned parallel to each other. The fine polishing was done using cloth and 0.05µm alumina polishing compound. All the polishing steps were done manually.

Samples were initially polished to 0.05µm, using ultrasonic cleaning in acetone and 90˚ rotations between each step to achieve a smooth surface. Starting from the smooth surface the sample was abraded with the sandpaper of interest and contact angle and roughness were measured.

2.2 Characterization

2.2.1 Oil/Water Contact Angle Measurement

The contact angles for all samples were measured at least five times by using Ramé-Hart Goniometer model 250 (Fig 2.1). To keep the environment consistent during the experiments all the samples were measured in cold tap water (10˚C).

Figure 2.1 Rame Hart Model 250Goniometer.

Oil/water contact angle was measured in a glass dish shown in Figure 2.2. The glass dish was filled with fresh water and the sample was kept on a sample holder. Vegetable oil

was injected by syringe on the bottom surface of sample as shown schematically in Figure 2.2. Before each contact angle measurement the sample, glass dish, and sample holder were cleaned with acetone to remove any contamination. Each measurement used fresh water to avoid error in the measurement.

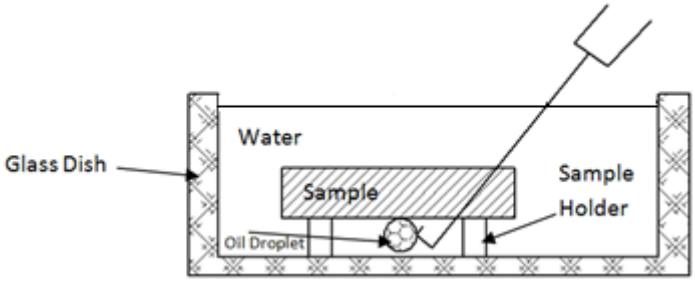

Figure 2.2. Schematic of oil/water contact angle measurement.

2.2.2 Surface Roughness Measurement

Surface roughness was measured by surface profilometer (Mitutoyo Surftest. 402) shown in Figure 2.3. Contact angle and roughness were measured at least 5 times on each samples and the average was calculated.

Figure 2.3.Surface profilometer (Mitutoyo Surftest. 402).

Agilent Technologies 5420 AFM, Atomic Force Microscope (AFM), (Figure 2.4) was used to study the topography of smooth surfaces. Nano-Indenter G200 was used to obtain the linear topography profile of rougher samples (Figure 2.5). Applied load was 30 μN and profile length was 200μm during the Nano-Indenter measurement.

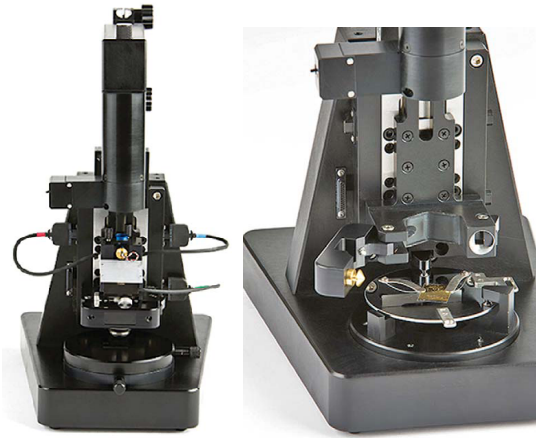

Figure 2.4. Image of Agilent Technologies 5420 AFM

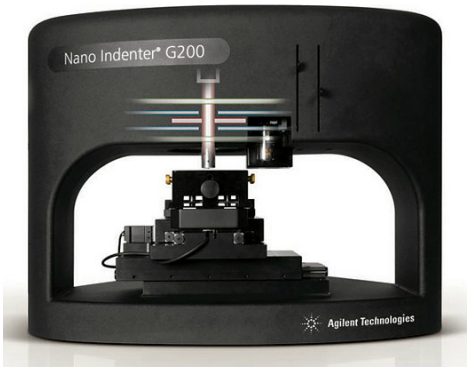

Figure 2.5. Image of Nano-Indenter G200.

Chapter 3

Modeling

3. Modeling

In this model it was assumed that the abrasive particles on the sand paper are arranged in a tightly packed simple cubic arrangement which produce scratches that are parallel to each other. The measured surface roughness (R_a) is assumed to be half the depth of scratches (i.e. actual depth of the scratches is $2R_a$). Additionally Figure 3.1 depicts the schematic of mechanical abrasion of samples. "D" is the abrasive particle diameter. "a" and "α" are geometrical parameters that depend on the depth of penetration of the abrasive particle into the substrate.

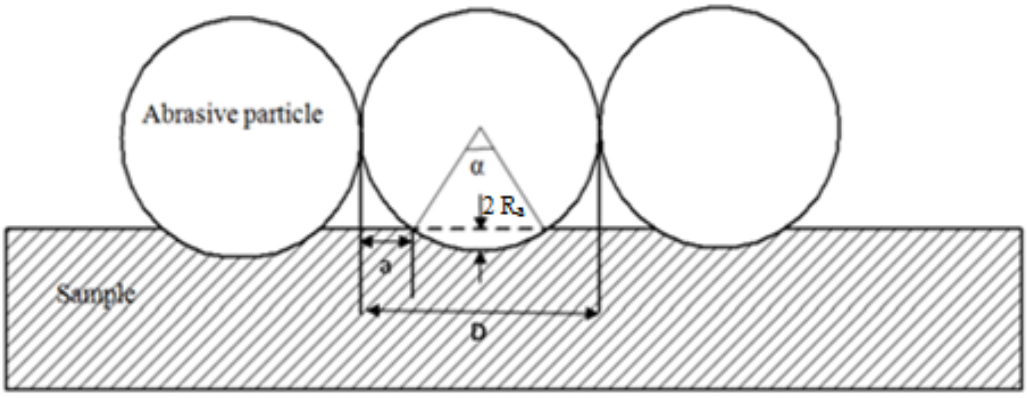

Figure 3.1. Schematic of mechanical abrasion.

The relationship between these geometrical parameters is described by Equation (3.1).

$$\frac{D}{2} = \frac{(D-2a)^2}{8(2R_a)} + \frac{2R_a}{2} = \frac{(D-2a)^2}{16\,R_a} + R_a \qquad (3.1)$$

Since D is a known property of the sandpaper and R_a is measured, the flat portion of the substrate, a, can be determined by rearranging Equation (3.1) as shown in Equation (3.2),

a= – - (3.2)

The angle α in Fig. 4.1 can be calculated by Equation 3.3.

$\alpha=2\sin^{-1}(1-$ —) (3.3)

Theoretically, in a water environment there are two conditions for an oil droplet on the surface. In the first, which is known as the Wenzel model, the entire oil droplet is in contact with substrate as shown in Figure 3.2a. In the second, there can be water present in gaps between droplet and the substrate as shown in Figure 3.2b. This is known as the Cassie-Baxter model.

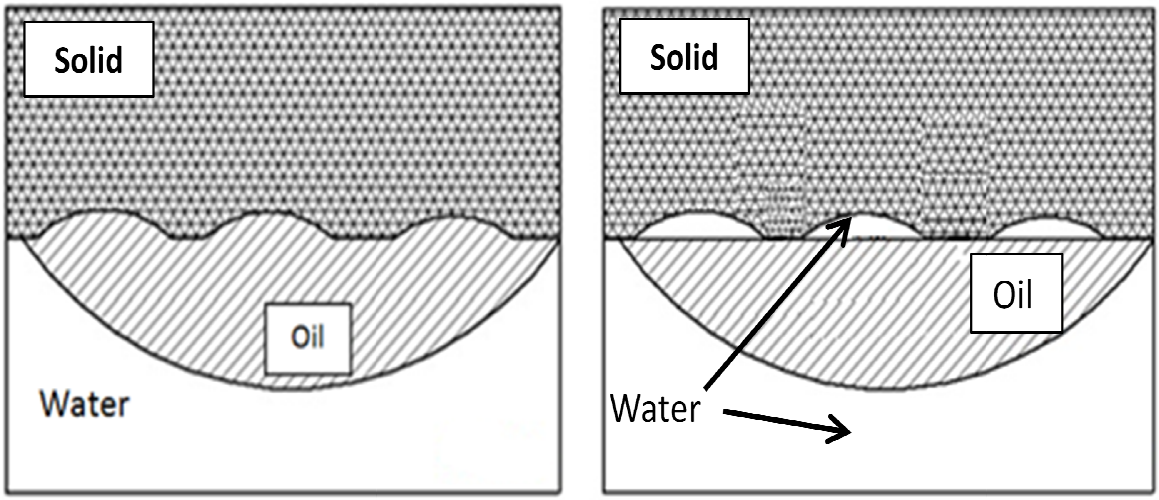

(a) (b)

Figure 3.2 Schematic of the two idealized system behaviors: a) Wenzel, entire surface in contact with oil, and b) Cassie-Baxter, surface in contact with both oil and water.

The roughness factor, R_f, is the ratio of the true area over projected area and can be calculated by Eq.3.4 for parallel scratches of length, L.

$$R_f = \frac{True\ Area}{Projected\ Area} = \frac{\left(2a + \pi D\frac{\alpha}{360}\right)L}{DL} = \frac{2a}{D} + \frac{\pi\alpha}{360} \quad (3.4)$$

The fraction of solid/oil interface, f_{SO}, can be calculated from equation 3.5.

$$f_{SO} = \frac{2a}{D} \quad (3.5)$$

Chapter 4

Results & Discussion

4. Results

4.1 Validation of Assumptions in Mechanical Abrasion Model

. The surface topography of stainless steel ground with 180, 320, and 800 were studied by nano indenter. It could be seen that some scratches are overlapped which is due to manual grinding. Surface topography of 180 grit abraded sample is shown in Figure 4.1.

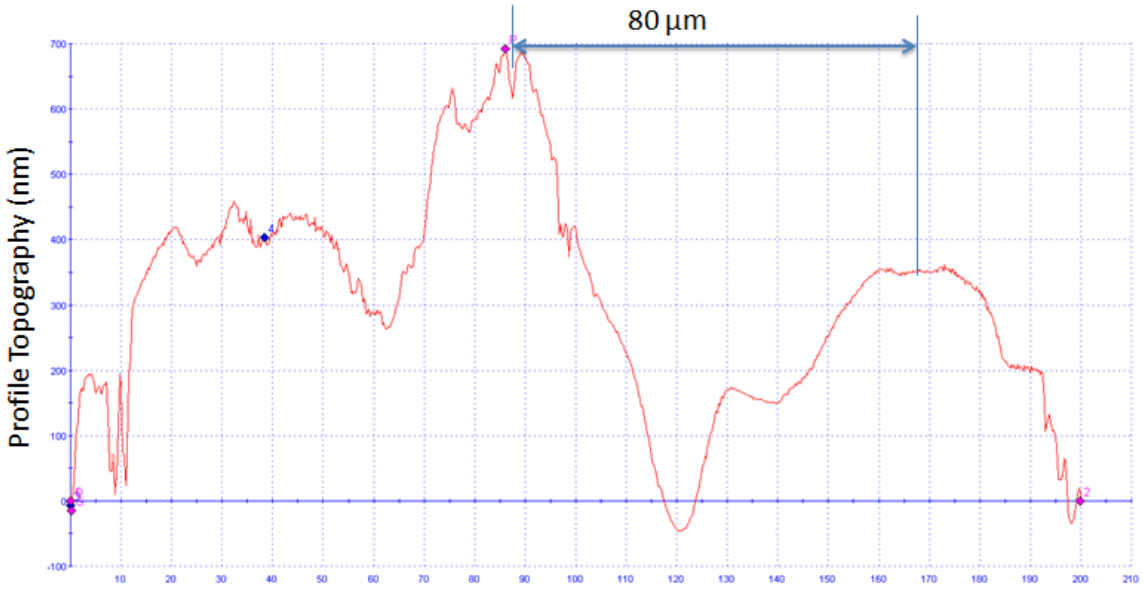

Figure 4.1 Nano-indention result for stainless steel abraded by 180grit sandpaper (D=80 µm)

Figure 4.2 depicts the nano-indenter results for stainless steel grinded with 320 grit sandpaper.

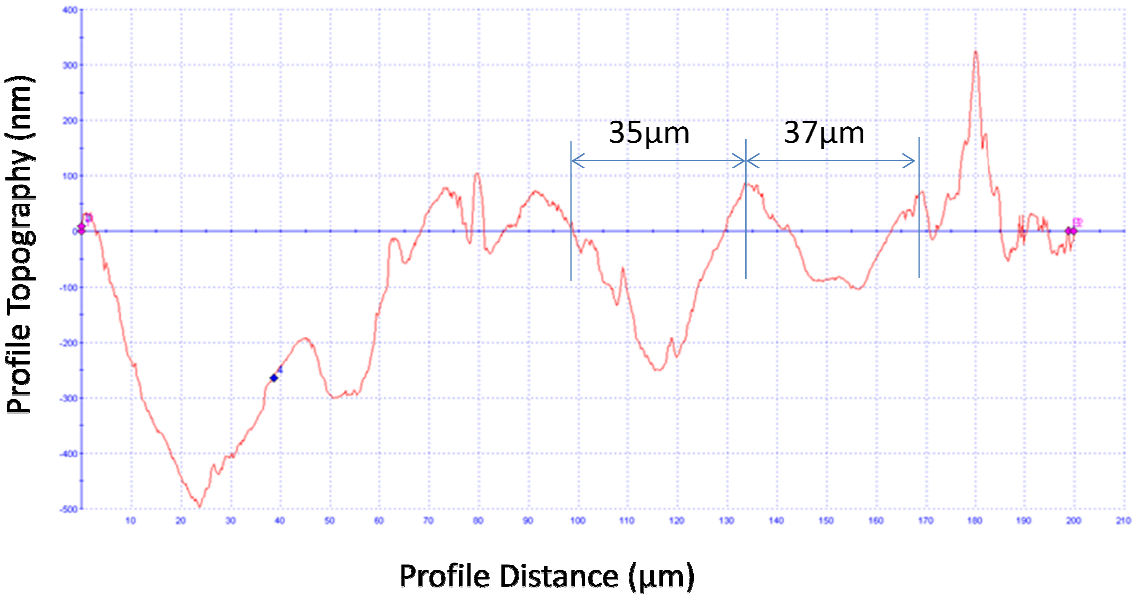

Figure 4.2. Nano-indention result for stainless steel abraded by 320 grit sandpaper (D=35µm).

Figure 4.3 shows that topography of scratches for sample abraded by 800 grit.

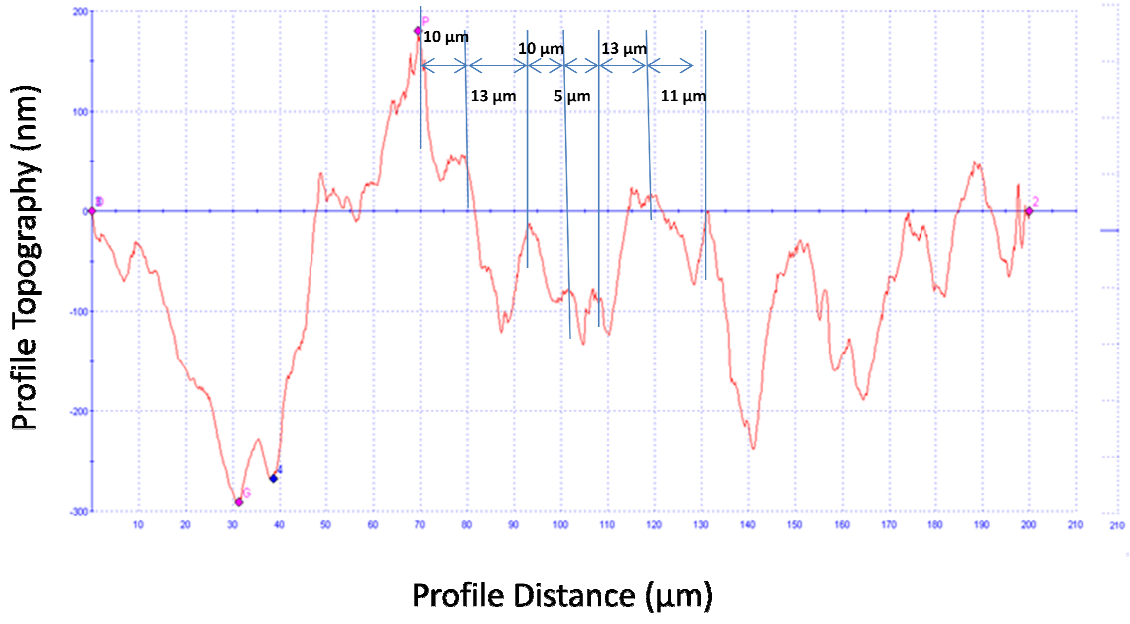

Figure 4.3. Nano-indention result for stainless steel abraded by 800 grit sandpaper (D=12.6 µm)

AFM analysis used for sample abraded by 800 sandpaper (Figure 4.4) showed that scratches are reasonably parallel which was the main assumption in the model presented in chapter 3.

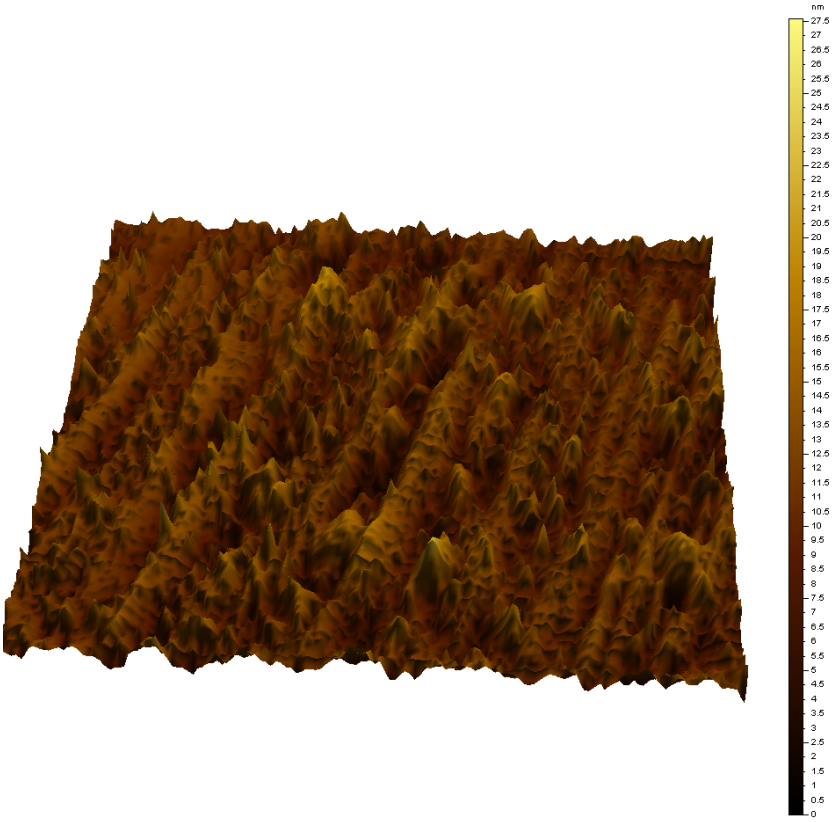

Figure 4.4. AFM image of stainless steel abraded by sandpaper grit 800.

AFM image of polished stainless steel with alumina is shown in Figure 4.5. Later it will be mentioned that to calculate the Cassie-Baxter predicted contact angle it will be assumed that polished sample has an R_f equal to one and here in this Figure 4.6 it is shown that sample has a very smooth surface. There a rough area in the right side of the image which could be due to damage during handling and it could be neglected.

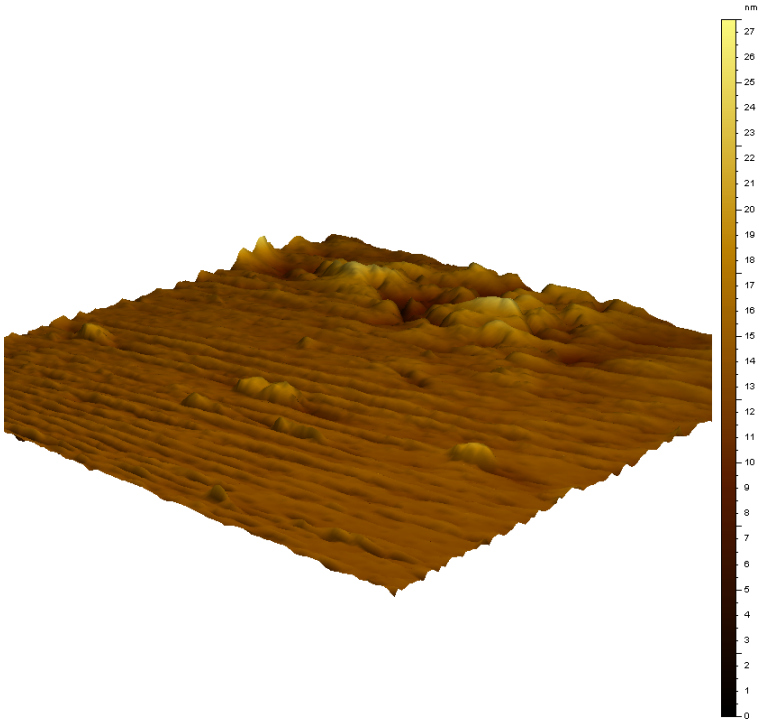

Figure 4.5. AFM image of stainless steel polished by alumina.

4.2Validation of Mechanical Abrasion Model

4.2.1 Brass

Brass samples were abraded mechanically to obtain parallel scratches on the surface.

In reality it is difficult to obtain a completely smooth surface. There is always some up and down on every surface. Figure 4.6 shows that the flat distance between two scratches on the sample is not actually flat. Since these small valleys are very shallow we can neglect them and assume the surface is flat.

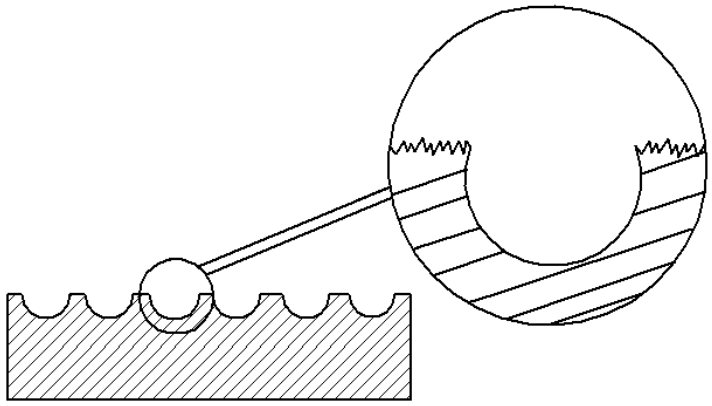

Figure 4.6.Schematic of surface after abrasion.

By the definition, R_f is surface area over flat projected area. Here, both flat area and projected area are same. As a result, roughness factor, $R_{f\ (CB)}$, for Cassie-Baxter model would be equal to one. This is shown below:

Surface area=$A_{\text{Solid/Oil}}$ L+ $A_{\text{Oil/Water}}$ L = 2aL + (D-2a) L=DL

Flat projected area = DL

$$R_{f\ (CB)} = \frac{\text{Surface area}}{\text{Flat projected area}} = 1$$

Table 1 indicates the oil contact angle (θ) in the water and surface roughness (R_a) of brass samples after grinding and polishing with different sand papers. According to the investigated model, there is a connection between sand paper's particle size (D), surface roughness and contact angle. In this table the theoretical measurement for roughness factor (R_f), fractional solid-oil contact area (f_{so}), Cos θ_w according to Wenzel model, and Cos θ_{CB} according to Cassie-Baxter model are presented. All the calculation is done according to the model in chapter 3.

Table 4.1 Measured and calculated values of contact angle for mechanical abrasive brass

Grit	D (μm)	R_a	$\theta_{oil/water}$	STD	Rf	f_{so}	Cos $\theta_{(measured)}$	Cos θ_w	Cos θ_{CB}
60	269	4.4	127.9	0.0295	1.007	0.644	-0.614	0.0277	-0.337
180	82	2	117.53	0.0692	1.014	0.569	-0.462	0.02788	-0.414
240	52.2	1.2	113.67	0.0916	1.013	0.581	-0.401	0.02785	-0.402
320	35	0.72	102.37	0.1319	1.011	0.603	-0.322	0.02779	-0.38
400	21.8	0.35	108.4	0.1195	1.007	0.647	-0.316	0.02769	-0.334
600	15.3	0.16	99.22	0.1971	1.004	0.714	-0.16	0.02759	-0.266
800	12.6	0.12	100.99	0.053	1.003	0.727	-0.191	0.02758	-0.253
1200	8.4	0.06	103.34	0.1327	1.002	0.763	-0.269	0.0275	-0.216
Alumina 0.05	0.05	0.03	88.42	0.091	1	1	0.028	0.028	0.028

According to the experiments, the sample which is polished by 0.05 μm alumina is considered the smooth sample. The oil contact angle (θ_0) measured on smooth surface was 88.42^0. Equation 4.1 and 4.2 are obtained by substituting this value in Wenzel and Cassie-Baxter equations.

$$\cos\theta_w = R_f \cos\theta_0$$

$$\cos\theta_w = R_f \cos 88.42 = 0.0275\, R_f \qquad (4.1)$$

$$\cos\theta_{CB} = f_{SO}\,(R_{f(CB)} \cos\theta_0 + 1) - 1$$

$$\cos\theta_{CB} = 1.0275 f_{SO} - 1 \qquad (4.2)$$

Figure 4.7 plots contact angle versus of R_f and f_{so} for Wenzel, Cassie-Baxter model and measured ones by the present experiments. It predicts that according to the Wenzel model, oil contact angle should stay almost constant while Cassie-Baxter shows a downward trend for cos θ. The experiment showed that experiment results of brass are close to the Cassie-Baxter model prediction when it is mechanically abraded.

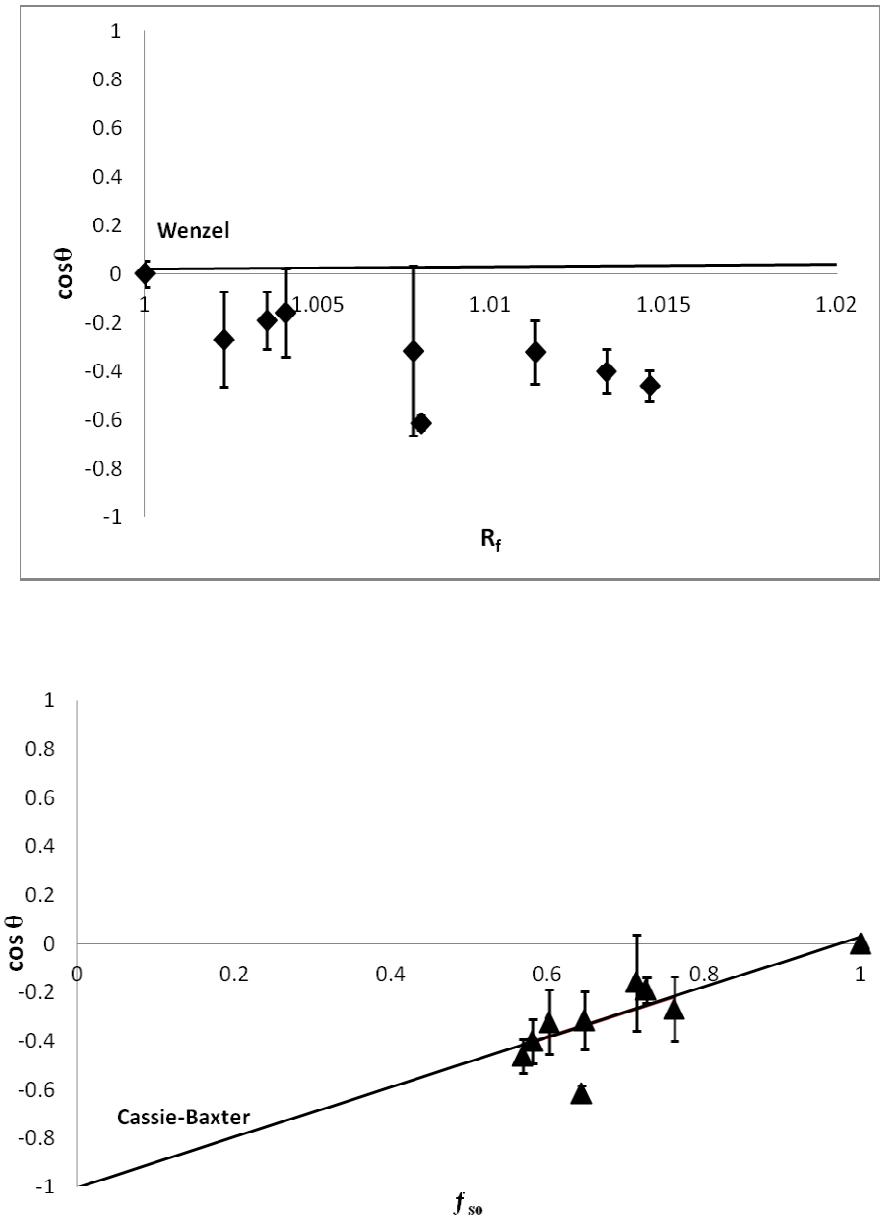

Figure 4.7. Comparison of Wenzel and Cassie-Baxter and experimental results for brass.

Figure 4.8 and Figure 4.9 show how sand paper grit size and particle size are related to the sample surface roughness. These two graphs indicate that rough sandpapers significantly affect the sample surface roughness. For smoother sandpapers there is only a slight change in samples surface roughness.

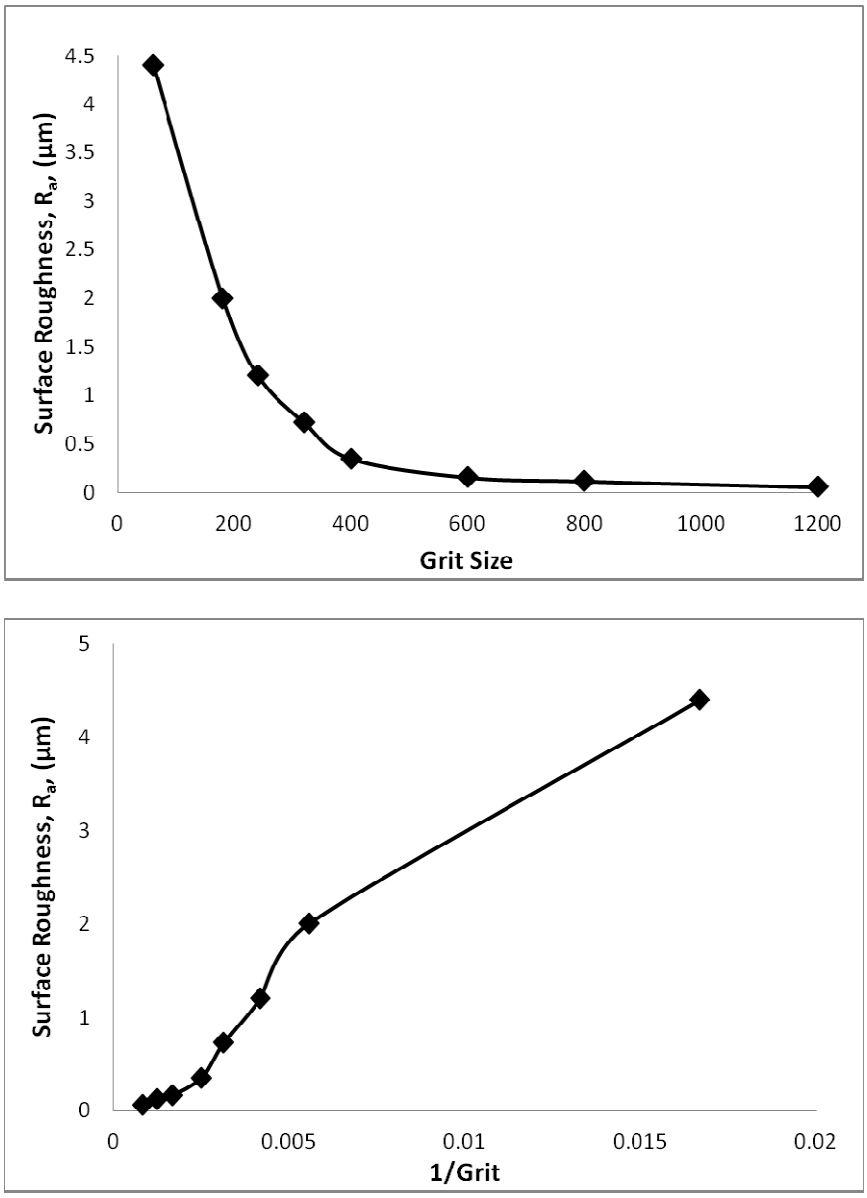

Figure 4.8 Effect of grit size on surface roughness.

Relation between surface roughness and sandpaper particle size is shown in Figure 4.9. Slope of changes is higher at larger particle size and slope decreases at smaller particles.

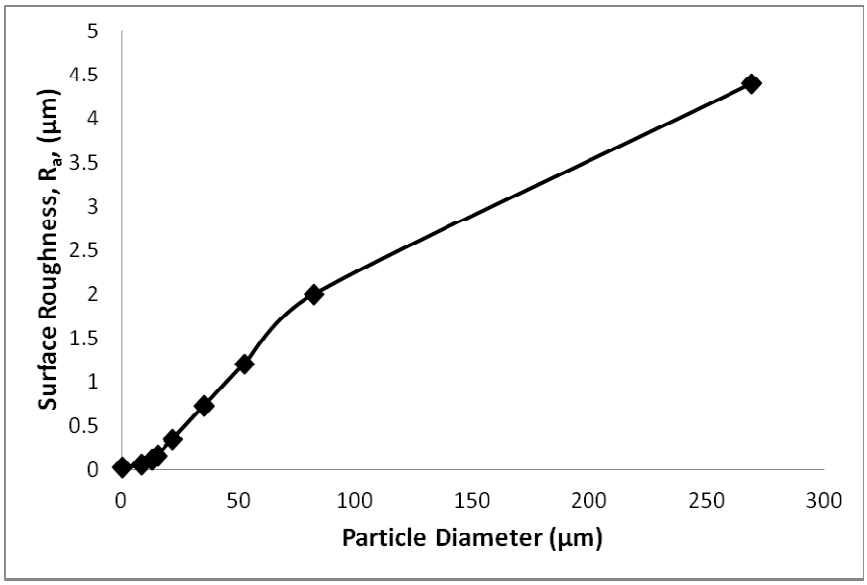

Figure 4.9 Sandpaper particle size against surface roughness.

To find an equation for changes of surface roughness by sandpaper particle size the logistics equation can be used. Logistic function equation is:

$$y = \frac{\quad}{\quad}$$

By normalizing, Figure 4.9 will change to Figure 4.10 which follows the logistic function. Here, A, B, and C are constant that are equal to 17.33, 0.0725, and 1.1, respectively. Logistic function for particle diameter versus surface roughness will follow the following equation:

$$R_a = \frac{\quad}{\quad} + 8.4\ D$$

where, D is sandpaper particle size.

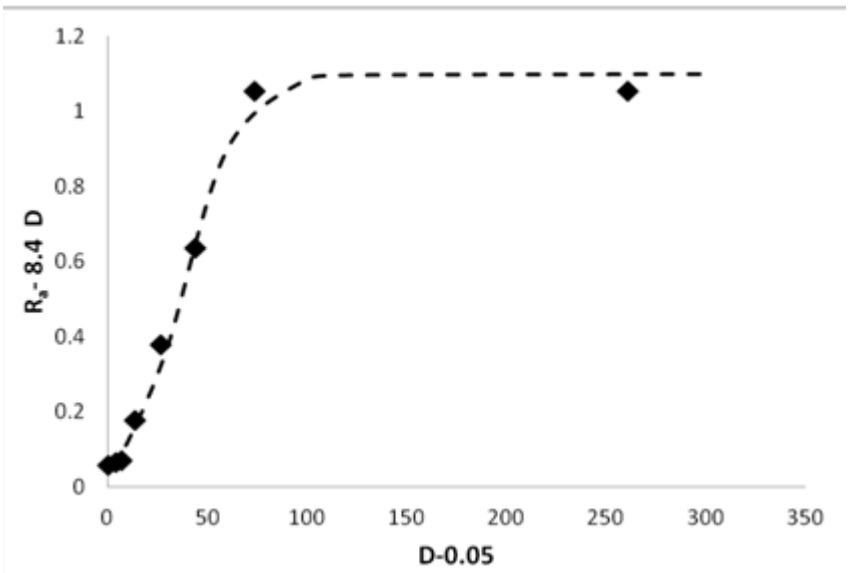

Figure 4.10. Logistic function for surface roughness against particle size.

Surface roughening is obtained by removing material from surface by sandpaper. Sandpaper particles should defeat the friction force and material removal. Both of these processes consume energy. Therefore, in a constant applied energy during grinding, extra energy after defeating friction will be used to remove the metal. When particle size is large, there is a higher surface in contact. As a result there is more friction which means less energy will remain to remove the metals. At medium size sandpaper particle, the friction energy is reduce due to less connection area which results in a transition in surface roughness between sandpaper grit 180 to 600. Again in small particles friction overcome the removing. This fact explains the changes in Figure 4.9.

Figure 4.11 plots the surface area of particles in contact with substrate against depth ($2R_a$) over width of scratch (D). Here in a constant length (500μm) number of available particles was calculated and the surface area on scratches was measured. This graphs shows a peak at 180 grit. This is an evidence explaining the transition in Figure 4.9 . There

is a peak at 180 grit sandpaper. In Figure 4.11 plot drops dramatically after 180 grit sandpaper too.

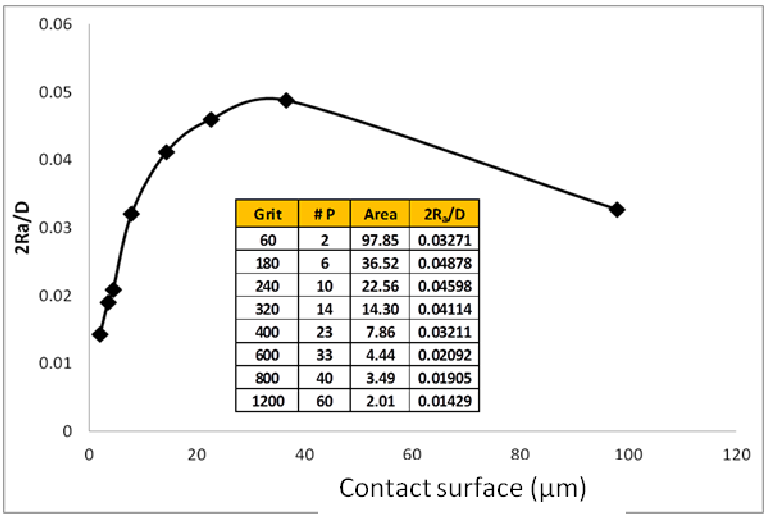

Grit	# P	Area	$2R_a/D$
60	2	97.85	0.03271
180	6	36.52	0.04878
240	10	22.56	0.04598
320	14	14.30	0.04114
400	23	7.86	0.03211
600	33	4.44	0.02092
800	40	3.49	0.01905
1200	60	2.01	0.01429

Figure 4.11. Relation between friction and material removal.

Figure 4.12 depicts the changes of contact angle with surface roughness. Plot shows that by increasing surface roughness increases contact angle.

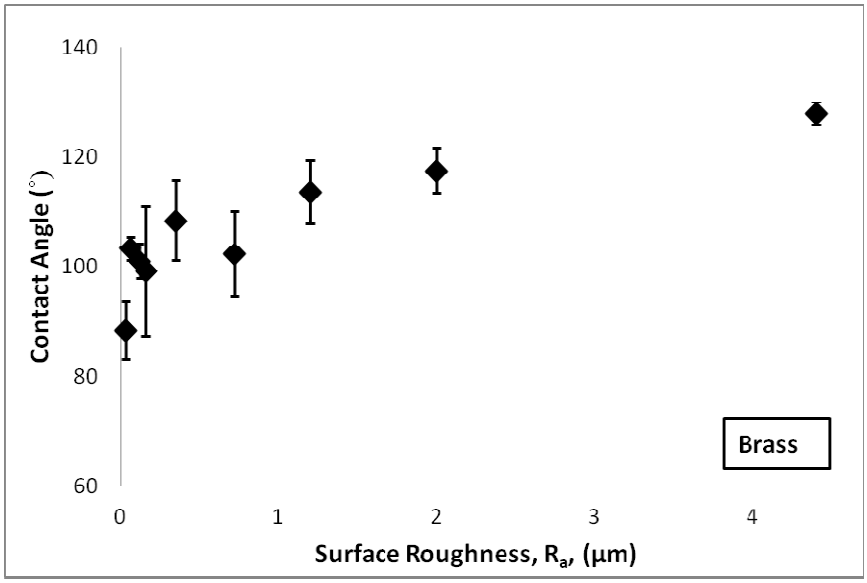

Figure 4.12. Effect of surface roughness on contact angle of brass.

4.2.2 Hastelloy C22

Hastelloy is the next metal that was chosen in the present research. Contact angle equations according to Wenzel and Cassie-Baxter will follow Eq. 4.3 and 4.4, respectively.

$$\cos\theta_w = R_f \cos\theta_0$$

$$\cos\theta_w = R_f \cos 97.01 = -0.122\, R_f \qquad (4.3)$$

$$\cos\theta_{CB} = f_{SO}\,(R_f \cos\theta_0 + 1) - 1$$

$$\cos\theta_{CB} = 0.878\ f_{SO} - 1 \qquad (4.4)$$

Table 4.2 lists values of contact angle (measured, Wenzel, and Cassie-Baxter), roughness factor, and f_{SO} at different grit sizes when all the scratches are parallel. Figure 4.13 compares the measured contact angles to Wenzel and Cassie-Baxter model.

Table 4.2 Predicted and measured data for hastelloy.

Grit	D(μm)	R_a (μm)	θ	R_f	f_{so}	cosθ(measured)	$\cos\theta_{CB}$	$\cos\theta_W$
180	82	0.64	109.00	1.0026	0.752	-0.3256	-0.217	0.04061
320	35	0.31	111.57	1.0032	0.736	-0.3677	-0.234	0.04063
600	15.3	0.07	113.61	1.0012	0.810	-0.4005	-0.158	0.04055
1200	8.4	0.035	87.68	1.0000	1	0.0405	0.041	0.04050

Figure 4.13 shows that experimental results follow the Cassie-Baxter model. All the measured values for hastelloy are very close to the Cassie-Baxter line.

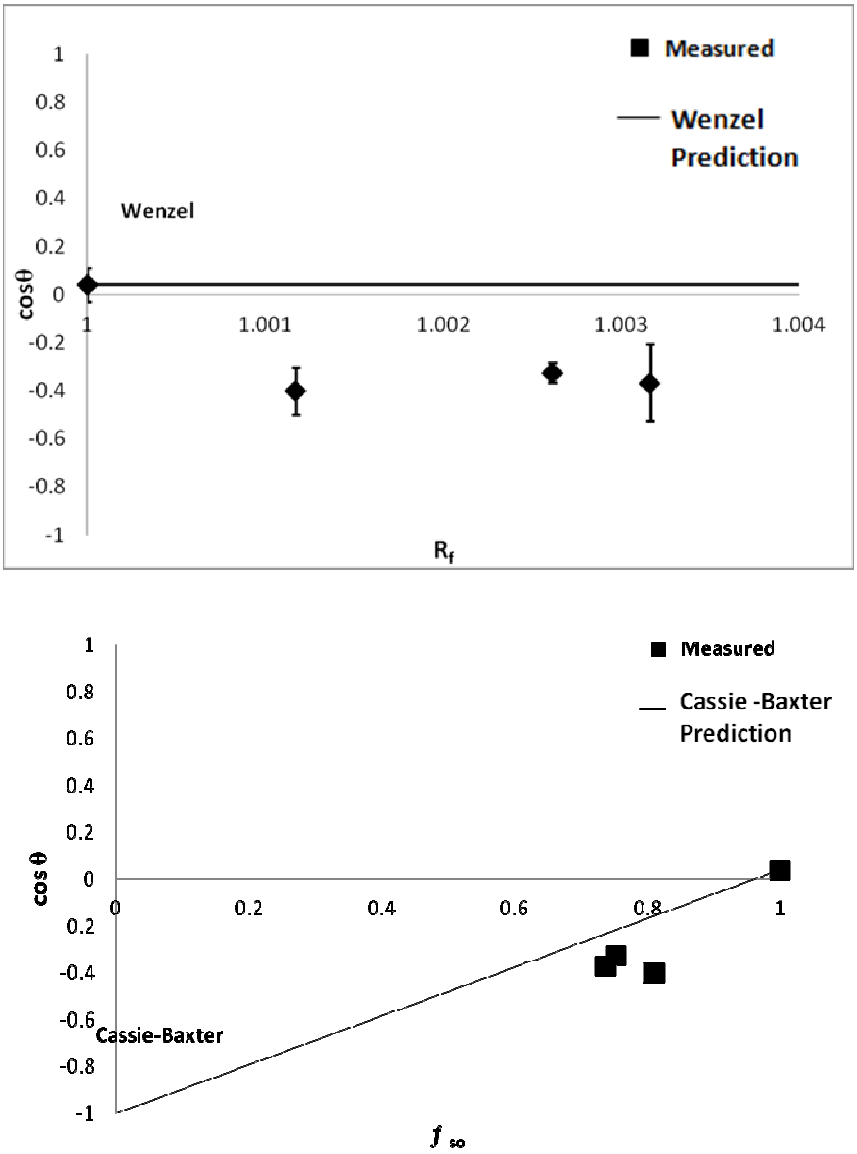

Figure 4.13 Comparison of measured contact angle with Wenzel and Cassie-Baxter models for Hastelloy.

Sandpaper particles size plotted against the surface roughness in Figure 4.14. Plot has two different slope at large and small particle sizes.

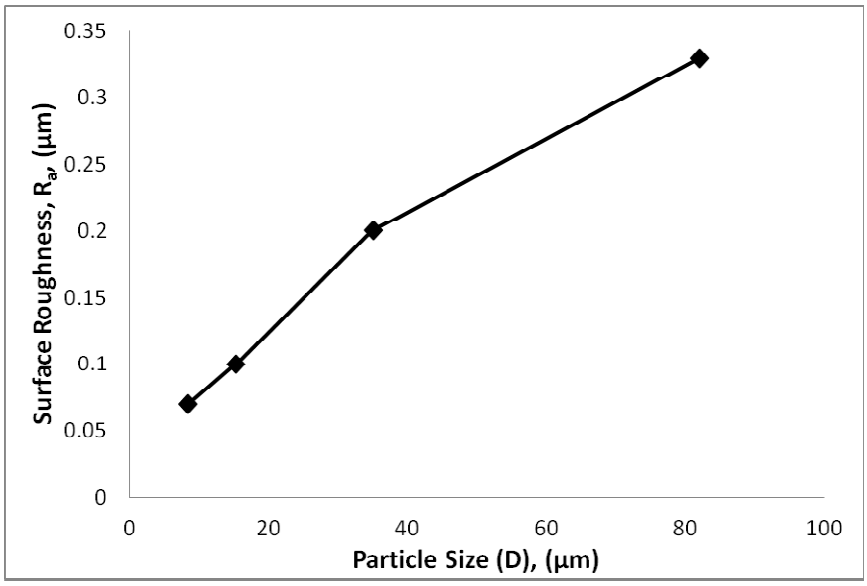

Figure 4.14. Effect of sandpaper particle size on surface roughness.

After normalizing the plot in Figure 4.14, the new graph follows the function with following equation:

$$R_a = \text{———————} + 0.0014\ D$$

The normalized plot with the corresponding logistic equation is shown in Figure 4.15. Presented data follow the logistic function very well.

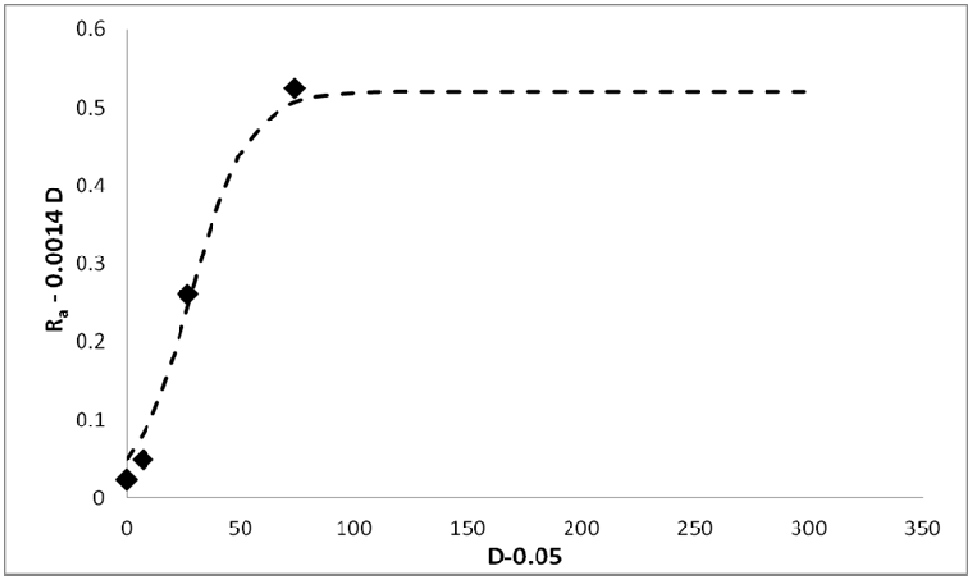

Figure 4.15. Normalized graph of sandpaper particle size against roughness.

Table 4.3 lists the surface roughness and contact angle at various grit size and sandpaper particle size and they are plotted in Figure 4.16.

Table 4.3. Data for parallel scratched hastelloy.

Grit	R_a	θ	STD
180	0.64	109.0	±0.04
320	0.31	111.6	±0.16
600	0.07	113.6	±0.09
1200	0.035	87.7	±0.07
Alumina	0.07	97.0	±0.06

Plotted results in Figure 4.16 indicate that contact angle decreases with decreasing the surface roughness.

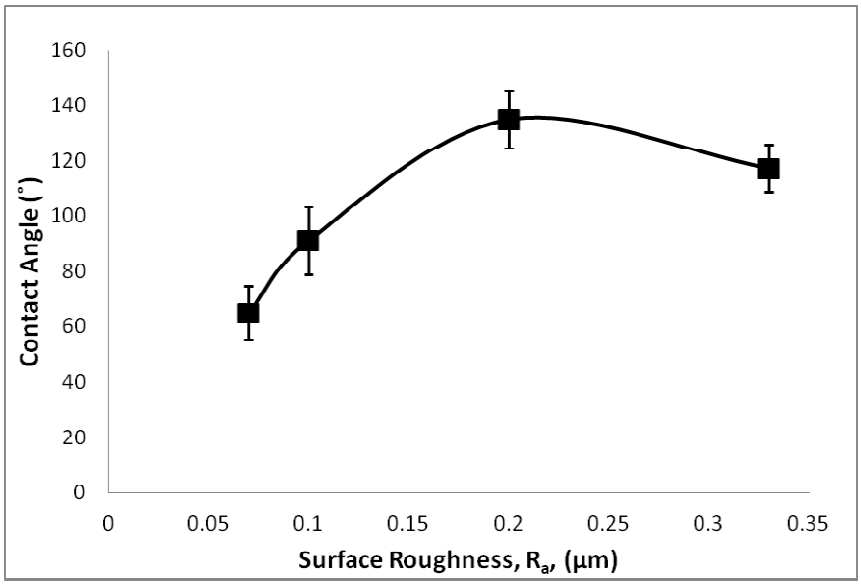

Figure 4.16. Effect of surface roughness on contact angle for parallel scratches hastelloy.

4.2.3 Aluminium

As it was discussed in section 5.1.1 for brass, roughness factor for aluminium sample in Cassie-Baxter model is one. Therefore the contact angle equations according to Wenzel and Cassie-Baxter will follow Eq. 4.5 and 4.6.

$$\cos\theta_w = R_f \cos\theta_0$$

$$\cos\theta_w = R_f \cos 121.98 = -0.529\, R_f \qquad (4.5)$$

$$\cos\theta_{CB} = f_{SO}\,(R_f \cos\theta_0 + 1) - 1$$

$$\cos\theta_{CB} = 0.47\, f_{SO} - 1 \qquad (4.6)$$

Table lists the values of contact angle (measured, Wenzel, and Cassie-Baxter) , roughness factor, and f_{SO} at different grit sizes.

Table 4.4 Measured and predicted data for Aluminium

Grit	D (μm)	R_a	θ oil/water	STD	R_f	f_{so}	Cos θ (measured)	Cos θ_w	Cos θ_{CB}
60	269	4.4	125.37	3.2	1.00797	0.644	-0.579	-0.534	-0.697
180	82	3.13	112.08	4.9	1.02880	0.469	-0.376	-0.545	-0.779
320	35	1.43	122.15	3.9	1.03194	0.452	-0.532	-0.547	-0.787
600	15.3	0.29	115.85	6.6	1.00996	0.618	-0.436	-0.535	-0.709
1200	8.4	0.14	108.27	4.2	1.00820	0.641	-0.313	-0.534	-0.698
Alumina	0.05	0.03	121.98	3.6	1.00000	1.000	-0.530	-0.530	-0.530

Figure 4.17 depicts the contact angles against fractional contact area. This graph shows Wenzel model and Cassie-Baxter predicted value too. It seems that experiment results follow Wenzel prediction.

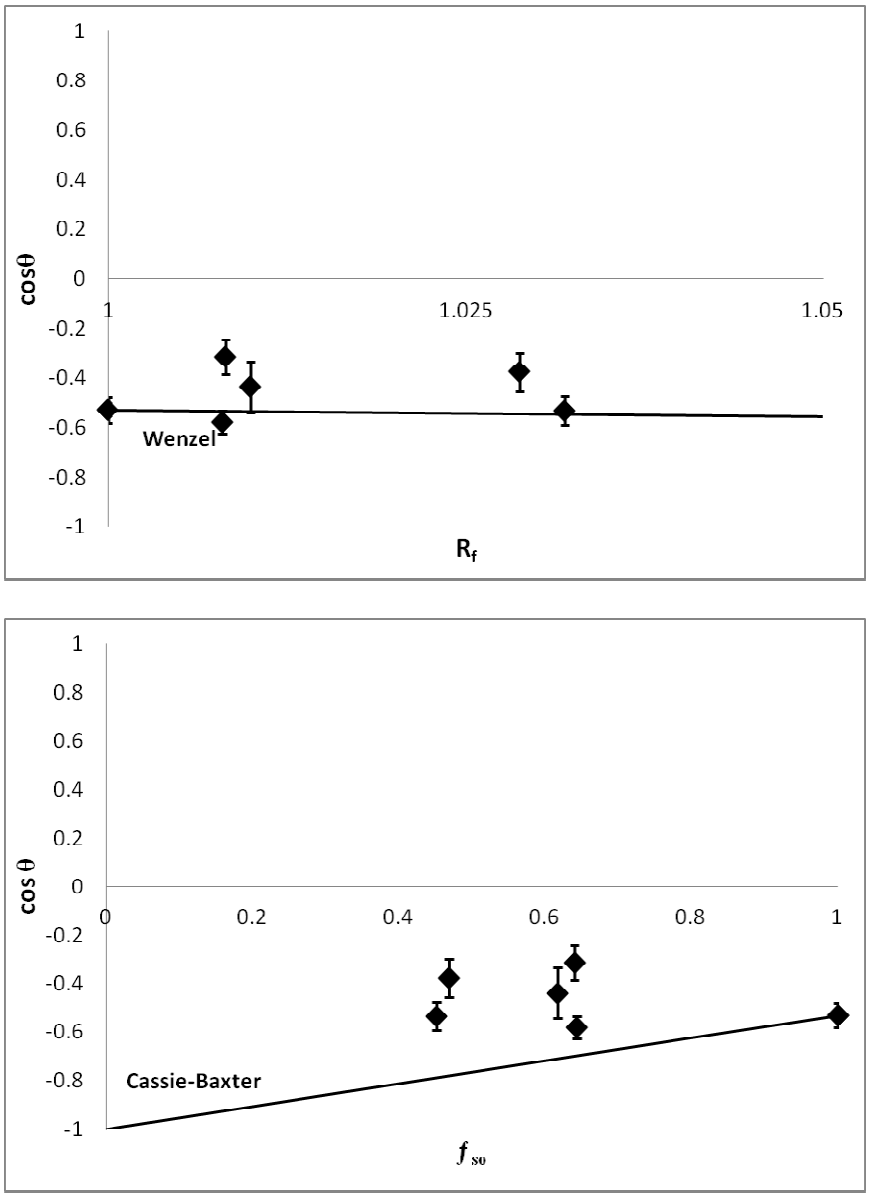

Figure 4.17. Comparison of Wenzel, Cassie-Baxter and experiment results for aluminium.

Relation between surface roughness of aluminium samples after grinding with sandpaper different particle size is shown in Figure 4.18 . It shows a transition again. This transition is happening between sandpaper grit 180 and 600, same as brass. As it was explained later, it could be due to the friction between sandpaper particles and substrate, and material removal.

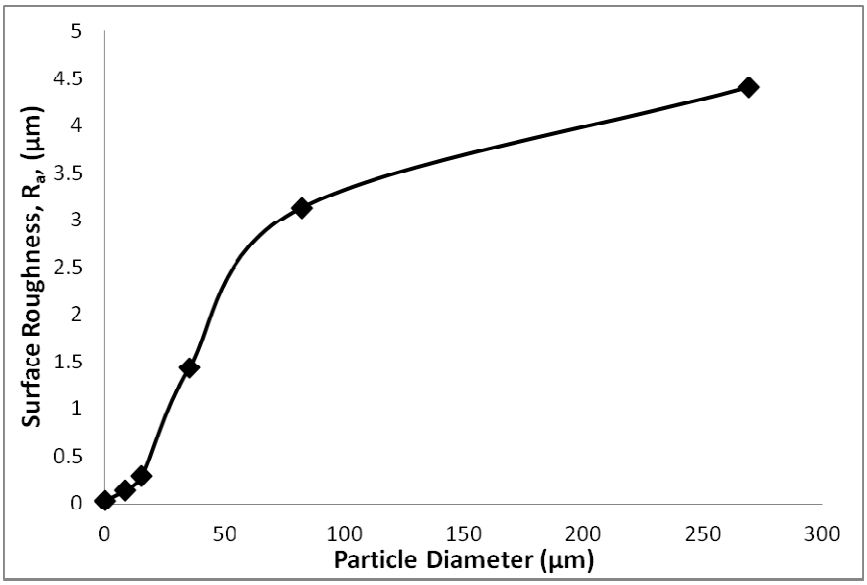

Figure 4.18. Changes of surface roughness by changing sandpaper particle size.

After normalizing the plot in Figure 4.18, the new one follows the logistic function with following equation:

$$R_a = \frac{\qquad}{\qquad} + 0.0067D$$

The normalized plot with the corresponding logistic equation is shown in Figure 4.19. Presented data follow the logistic equation very well.

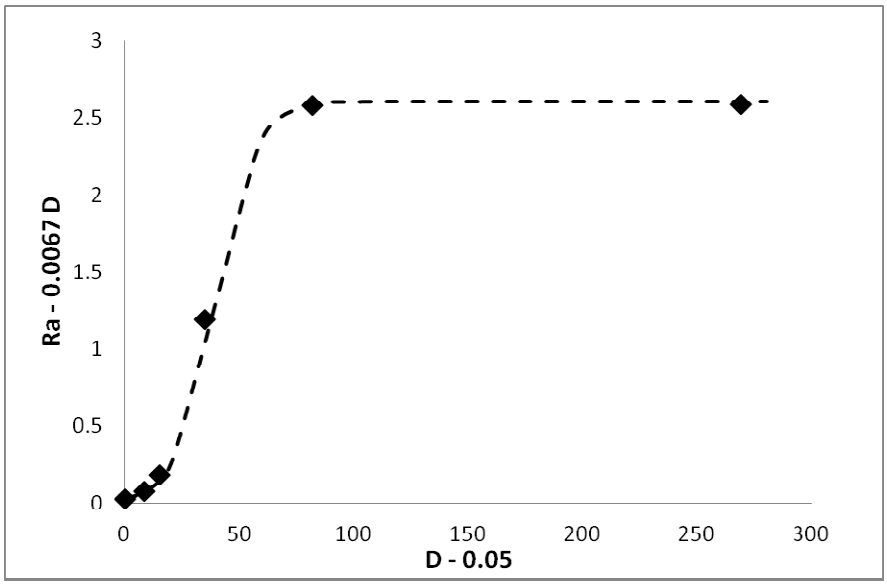

Figure 4.19. Normalized plot of particle size and surface roughness for aluminium.

Average measured contact angle on samples that grinded with different sandpaper grits are plotted in Figure 4.20.According to Wenzel model [1] at contact angle higher than 90˚, contact angle increases with increasing the surface roughness. Here, experiment results show this increases.

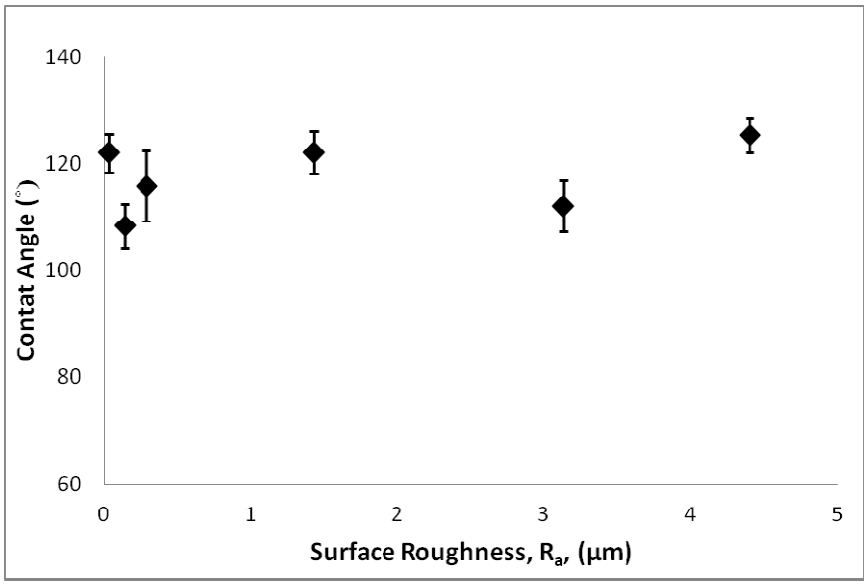

Figure 4.20. Contact angle at surface roughness.

4.2.4 Stainless Steel 316

Predicted contact angle for stainless steel according to Wenzel and Cassie-Baxter model are calculated by Equation 4.7 and 4.8.

$$\cos \theta_w = R_f \cos\theta_0$$

$$\cos \theta_w = R_f \cos 82.98 = 0.1222\ R_f \qquad (4.7)$$

$$\cos \theta_{CB} = f_{SO} (R_f \cos \theta_0 + 1) - 1$$

$$\cos \theta_{CB} = 1.122\ f_{SO} - 1 \qquad (4.8)$$

All the measured and predicted value for contact angle at different grit sizes are shown in Table 4.5.

Table 4.5 Measured and calculated data for stainless steel

Grit	D (μm)	R_a (μm)	θ	STD	R_f	f_{so}	$\cos\theta_{(measured)}$	$\cos\theta_W$	$\cos\theta_{CB}$
60	269	1.23	76.94	10.32	1.001169	0.8096	0.2260	-0.320	-0.449
180	82	0.66	89.26	3.22	1.002736	0.7483	0.0129	-0.320	-0.491
320	35	0.44	94.33	5	1.005356	0.6869	-0.0755	-0.321	-0.533
800	12.6	0.11	82.98	4.02	1	0.738	0.1222	-0.319	-0.498

Figure 4.21 plots measured contact angle variation with R_a as well as the prediction of both the Wenzel and Cassie-Baxter models. Figure 4.21 shows that sample which has a low smooth surface contact angle seems to sometimes follow Wenzel and sometimes Cassie Baxter, but there is no clear transition behavior.

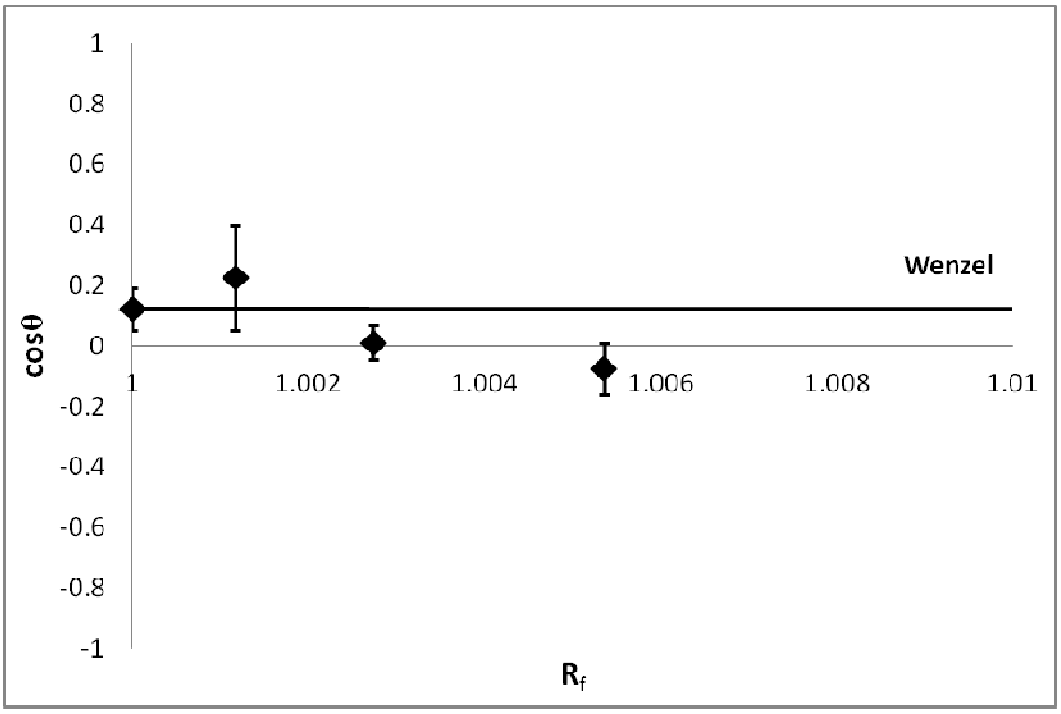

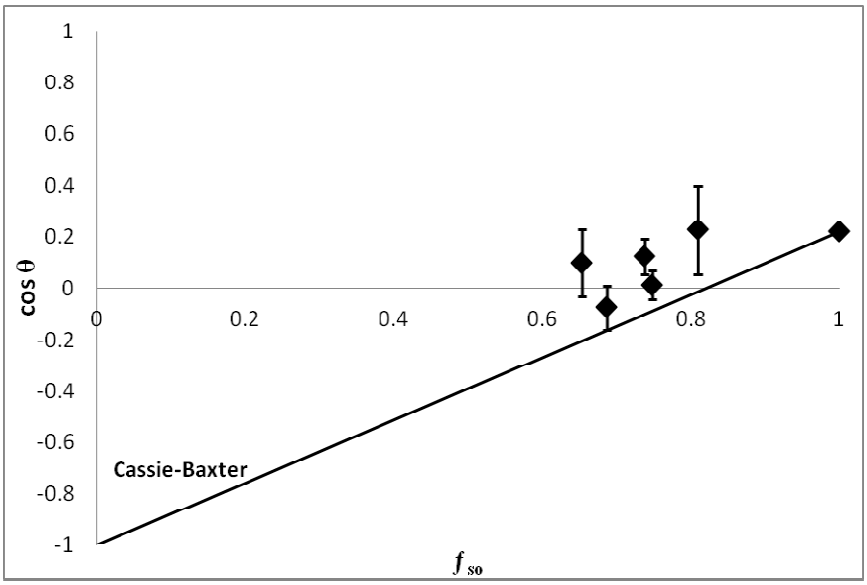

Figure 4.21 Comparison of experimental results with Wenzel and Cassie-Baxter predictions for stainless steel

Relation between surface roughness of stainless steel samples after grinding with sandpaper different particle size is shown in Figure 4.22. It shows a transition again. This transition is happening between sandpaper grit 180 and 600, same as brass. Surface roughness has a following relation to particle size:

$$R_a = \text{————————} + 0.04\ D$$

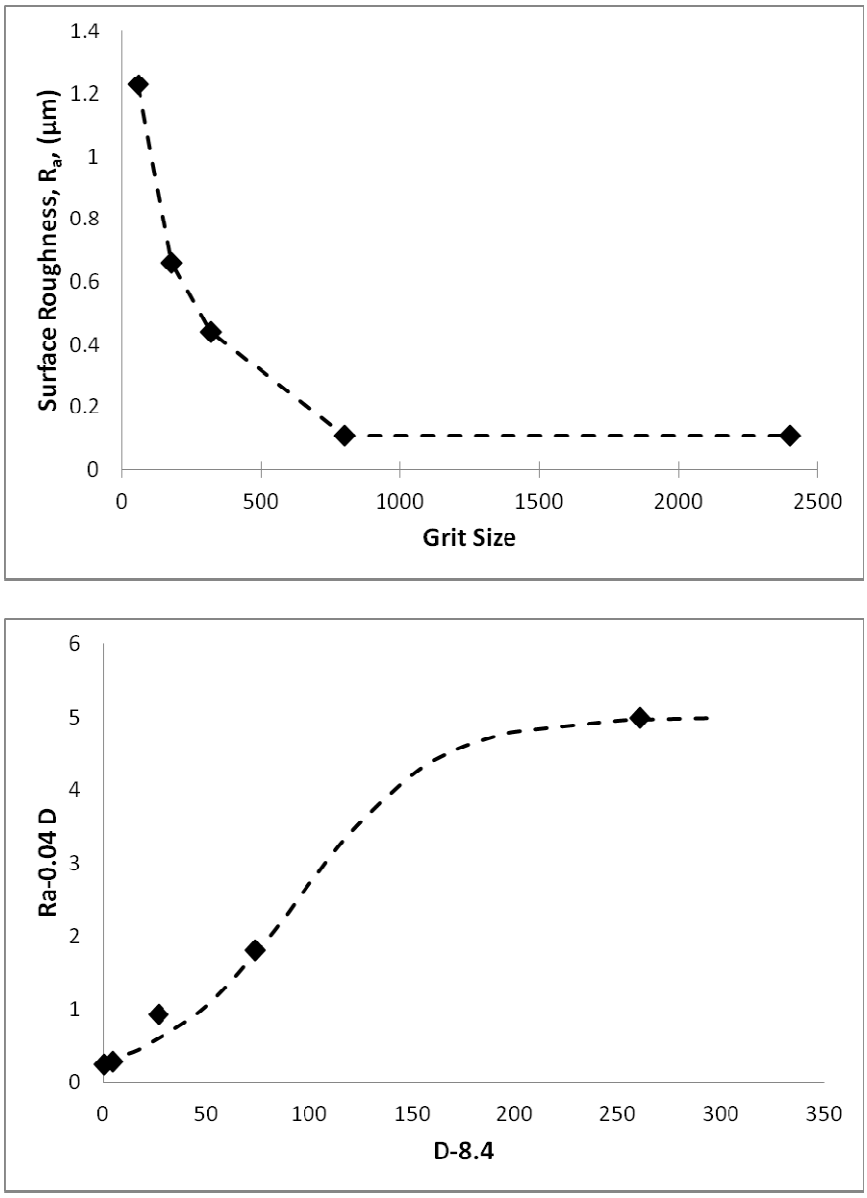

Figure 4.22 Surface roughness changes with changing sandpaper grit for stainless steel.

Contact angle at different surface roughness are shown in Figure 4.23. It was observed that contact angle increases with increasing the surface roughness and after reaching a maximum it drops again.

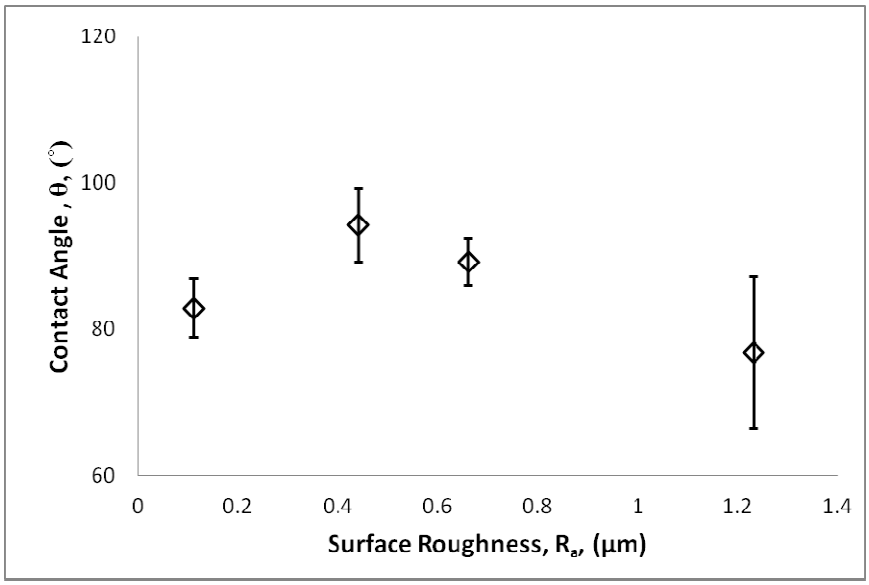

Figure 4.23. Contact angle at different surface roughness of stainless steel.

The slope of f_{so} versus $\cos\theta_0$ will be calculated by following equation:

——— = ——— =

Figure 4.24 plots the variation of for the Cassie-Baxter model with as well as the experimentally determined slope. It can be seen that are three regions in this plot. Brass and Hastelloy fall in Cassie-Baxter region, while aluminum falls in the Wenzel section. Stainless Steel seems to exhibit mixed behavior between the Wenzel and Cassie-Baxter models and probably marks the boundary between the two types of behavior. From symmetry it is assumed that the boundary for high θ_0 metals is slightly more than 100^o.

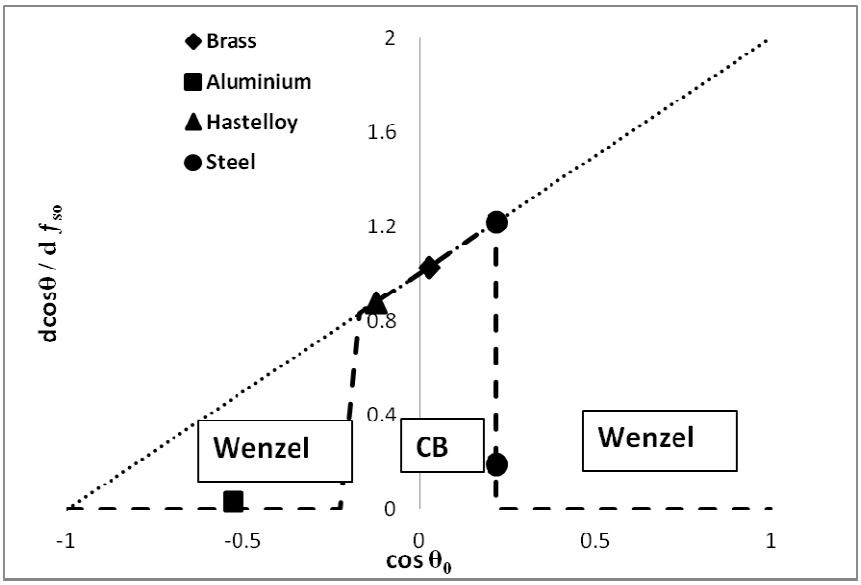

Figure 4.24. Location of different metal in Wenzel and Cassie-Baxter section.

Conclusions

1. Oil/water contact angle of oil on brass on fine polished (using 0.05μm Al_2O_3) surface increases from 88˚ with increasing the surface roughness and reaches 128 ˚ on 60 Grit polishing paper.

2. Contact angle of fine polished hastelloy (97˚) is less than that of the rough sample (~ 113˚)

3. Contact angle of oil on fine polished aluminium decrease from 122˚ to 108 ˚ on 1200 grit and then increases with further increasing the surface roughness to 125˚ on 60 grit.

4. Contact angle of oil on steel increases from 83˚ on fine polished surface to 97˚ on sample polished with 320 grit paper, and then decreases with increasing the surface roughness and reaches 77˚ on sample polished with 60 grit paper.

5. Increases of surface roughness with increases sandpaper particle size has been quantified for all four metals.

6. A model has been developed to calculate R_f and f_{so} and these have been used to predict contact angle for Wenzel and Cassie-Baxter type of behavior.

7. Brass and hastelloy demonstrate Cassie-Baxter behavior.
8. Aluminum seems to follow the Wenzel model.
9. Stainless steel shows a transition from Wenzel at low R_f to Cassie-Baxter at higher R_f.

References

[1] M. Nosonosvsky and B. Bhushan, "Roughness optimization for biomimetic superhydrophobic surfaces," *Microsyst,* vol. 11, pp. 535-549, 2005.

[2] Y. C. Jung and B. Bhushan, "Contact angle, adhesion and friction properties of micro- and nanopatterned polymers for superhydrophobicity," *Nanotechnology*, vol. 17, pp. 4970-4980, 2006.

[3] D. Quere, A. Lafuma and J. Bico, "Slippy and sticky microtextured solids," *Nanotechnology,* vol. 14, pp. 1109-1112, 2003.

[4] J. Genzer and K. Efimenko, "Recent developments in superhydrophobic surfaces and their relevance to marine fouling: a review," *Biofouling*, vol. 22, no. 5, pp. 339-360, 2006.

[5] G. G. Adamson, Physical Chemistry of Surfaces, New York: Wiley, 1990.

[6] B. Bhushan, Introduction to Tribology, Wiley, 2002.

[7] T. Young, *trans.R.Soc'London,* vol. 95, p. 65, 1805.

[8] J. S. Rowlinson and B. Widom, Molecular theoery of Capillarity, Oxford: Clarendon, 1982.

[9] A. B. Ponter and A. P. Boyes, *Canad.J.Chem,* vol. 50, p. 2419, 1972.

[10] M. Nosonovsky and B. Bhushan, Multiscale Dissipative Mechanisms and hierarchical Surfaces, New York: Springer, 2008.

[11] D. Li, A. Neumann and A. W. Newumann, "Effect of Corrugations of the three-Phase Line

on the Drop Size Dependence of Contact ANgles," *Journal of Colloid and Interface Science,* vol. 142, no. 1, p. 224, 1991.

[12] P. Letellier, A. Mayaffre and M. Turmine, "Drop size effect on contact angle explained by nonextensive thermodynamics. Young's equation revisited," *Journal of Colloid and Interface Science,* vol. 314, pp. 604-614, 2007.

[13] V. Hejazi and M. Nosonovsky, "Wetting Transitions in Two-, Three-, and Four-Phase Systems," *langmuir,* vol. 28, pp. 2173-2180, 2012.

[14] R. N. Wenzel, "Resistance of solid surfaces to wetting by water," *Insustrial and engineering chemistry,* vol. 28, no. 8, pp. 988-994, 1936.

[15] A. B. Cassie and S. Baxter, "Wettability of porous surfaces," *Transactions of the Faraday Society,* vol. 40, p. 546, 1944.

[16] L. Gao and T. J. McCarthy, "How Wenzel and Cassie Were Wrong," *Langmuir,* vol. 23, pp. 3762-3765, 2007.

[17] G. Mchale, "Cassie and Wenzel:Were They Really Sp Wrong?," *Langmuir,* vol. 23, pp. 8200-8205, 2007.

[18] E. S. Savoy and F. A. Escobedo, "Molecular Simulations of Wetting of a Rough Surface by an Oily Fluid:Effect of Topolory, Chemistry ,and Droplet Size on Wetting Transition Rate," *Langmuir,* vol. 28, pp. 3412-3419, 2012.

[19] E. G. Shafrin and W. A. Zisman, "Constitutive relations in the wetting of loe energy surfaces and the theory of the retraction method of preparating monolayers," *J. Phys. Chem.,* vol. 64,

no. 5, pp. 519-524, 1960.

[20] P. Tsai, S. Pacheco, C. Pirat and D. Lohse, "Drop Impact upon Micro- and Nanostructured Superhydrophobic Surfaces," *Langmuir,* vol. 25, p. 12293, 2009.

[21] G. Manukyan, J. M. Oh, D. van den Ende and F. Mugele, "Electric-field–driven instabilities on superhydrophobic surfaces," *Phys. Rev. Lett.*, vol. 93, p. 56001, 2011.

[22] J. Drelich, J. D. Miller and J. Hupka, "the effect of Drop Size on Contact Angle over a Wide Range of Drop Volumes," *Journal of Colloid and Interface Science,* vol. 155, no. 2, pp. 379-385, 1993.

[23] R. J. Good and M. N. Koo, "The effect of drop Size on Contact Angle," *J. of Cooloic and Interface Science,* vol. 71, no. 2, pp. 283-292, 1979.

[24] H. Wang, Y. Xue and T. Lin, *Soft Matter,* vol. 7, p. 8158, 2011.

[25] M. Nosonovsky and B. Bhushan, "Patterned Non-Adhesive Surfaces: Superhydrophobicity and Wetting Regime Transitions," *Langmuir,* vol. 27, p. 14419, 2011.

[26] Y. Liu, Y. Xiu, D. W. Hess and C. P. Wong, "Silicon Surface Structure-Controlled Oleophobicity," *Langmuir*, vol. 26, no. 11, pp. 8908-8913, 2010.

[27] A. Steele, I. Bayer and E. Loth, "Inherently Superoleophobic Nanocomposite Coatings by Spray Atomization," *Nano Lett,* vol. 9, no. 1, pp. 501-505, 2009.

[28] R. Campos, A. J. Guenthner, A. J. Meuler, A. Tuteja, R. E. Cohen, G. H. McKinley, T. S. Haddad and J. M. Mabry, "Superoleophobic Surfaces through Control of Sprayed-on Stochastic Topography," *Langmuir,* 2012.

[29] S. R. Coulson, I. S. Woodward and J. P. Badyal, "Ultralow Surface Energy Plasma Polymer Films," *Chem. Mater,* vol. 12, pp. 2031-2038, 2000.

[30] Y. Coffinier, S. Coffinier, A. Addad, R. Blossey, L. Gengembre, E. Payen and R. Boukherroub, "Preparation of superhydrophobic silicon nanowires surfaces," *Langmuir,* vol. 23, pp. 1608-1611, 2007.

[31] L. Cao, T. P. Price, M. Weiss and D. Gao, "Super Water- and Oil-Repellent Surfaces on Intrinsically Hydrophilic and Oleophilic Porous Silicon Films," *Langmuir*, vol. 24, pp. 1640-1643, 2008.

[32] R. T. Kumar, K. B. Mogensen and P. Bøggild, "Simple Approach to Superamphiphobic Overhanging Silicon Nanostructures," *J. Phys. Chem.,* vol. 114, pp. 2936-2940, 2010.

[33] R. Campos, A. J. Guenthner, A. J. Meuler, A. Tuteja, R. E. Cohen, G. H. McKinley, T. S. Haddad and J. M. Mabry, "Superoleophobic Surfaces through Control of Sprayed-on Stochastic Topography," *Langmuir,* 2012.

[34] "Facile Means of Preparing Superamphiphobic Surfaces on Common Engineering Metals," *J. Phys. Chem. ,* vol. 112, pp. 11454-11458, 2008.

[35] D. Han and A. J. Steckl, "Superhydrophobic and Oleophobic Fibers by Coaxial Electrospinning," *Langmuir,* vol. 25, no. 16, pp. 9454-9462, 2009.

[36] Cassie and Baxter.

[37] R. N. Wenzel, "Resistance of Solid Surfaces to Wetting by Water," *Industrial and Engineering Chemistry,* vol. 28, no. 8, pp. 988-994, 1936.

[38] L. Gao and J. McCarthy, "How Wenzel and Cassie Were Wrong," *Langmuir*, vol. 23, pp. 3762-3765, 2007.

[39] G. McHale, "Cassie and Wenzel:Were They Really Sp Wrong?," *Langmuir*, vol. 23, pp. 8200-8205, 2007.

APPENDIX 1:

Hastelloy -Optical microscopic images (50 x)

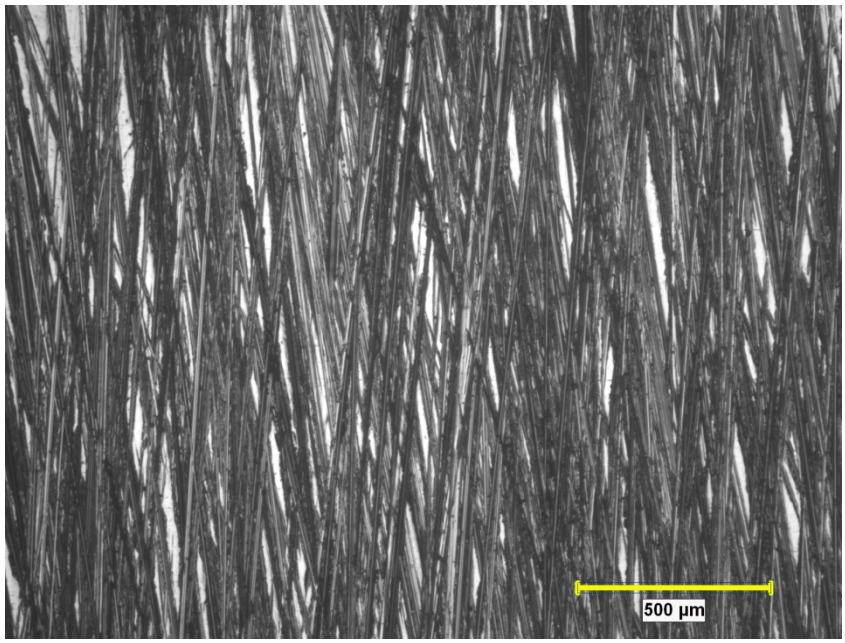

60 Grit

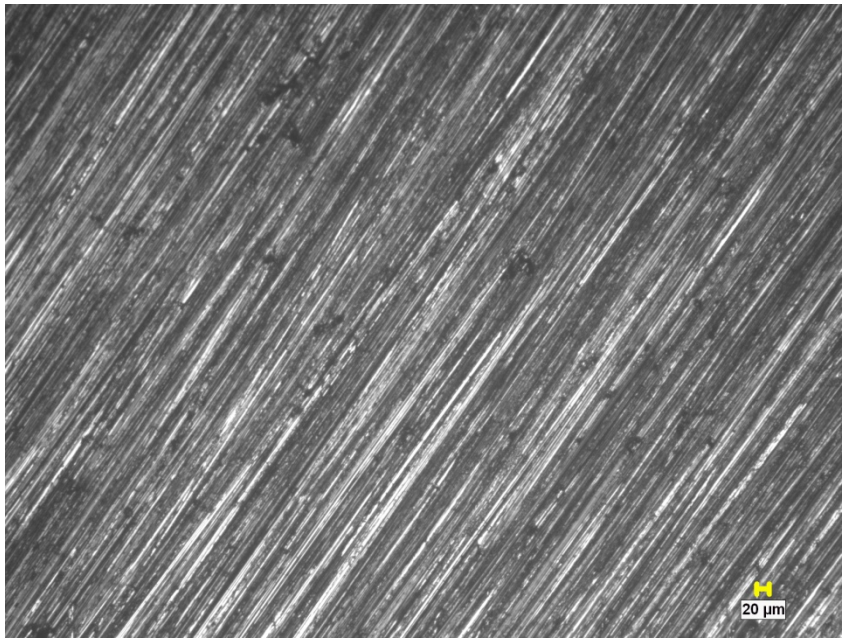

180 Grit

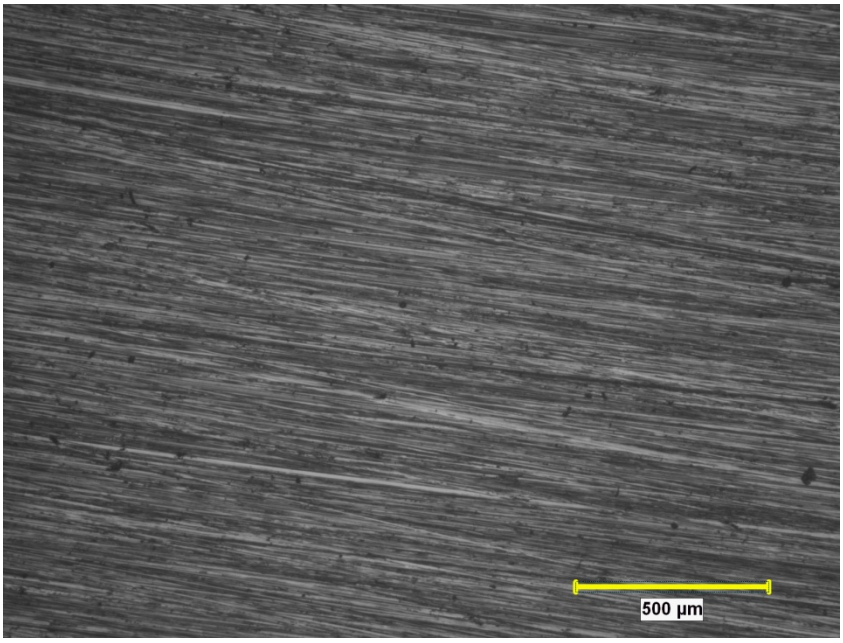

240 Grit

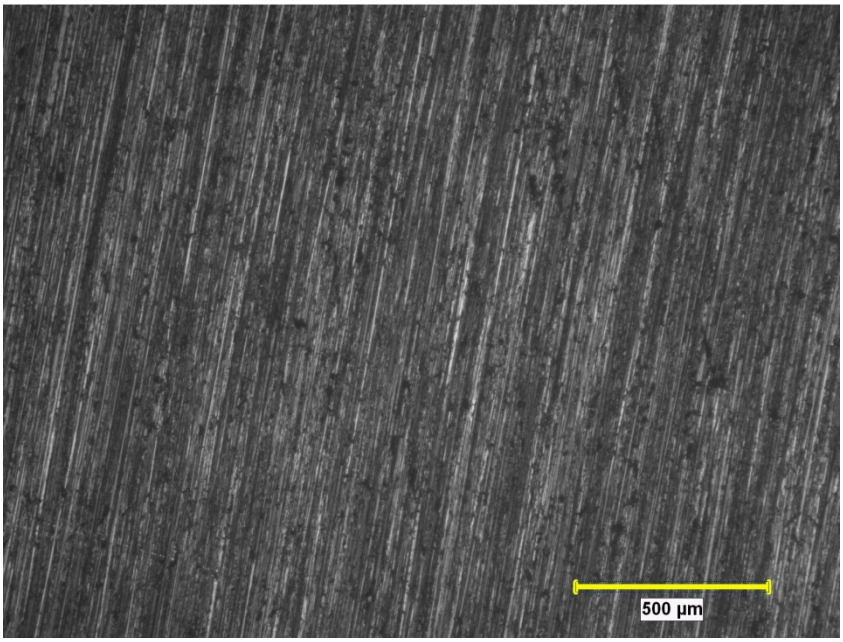

320 Grit

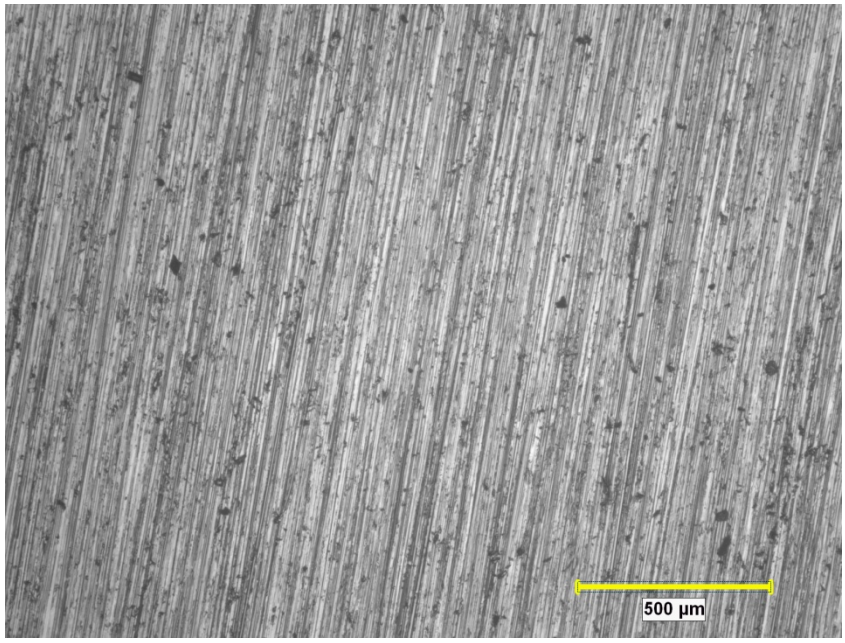

600 Grit

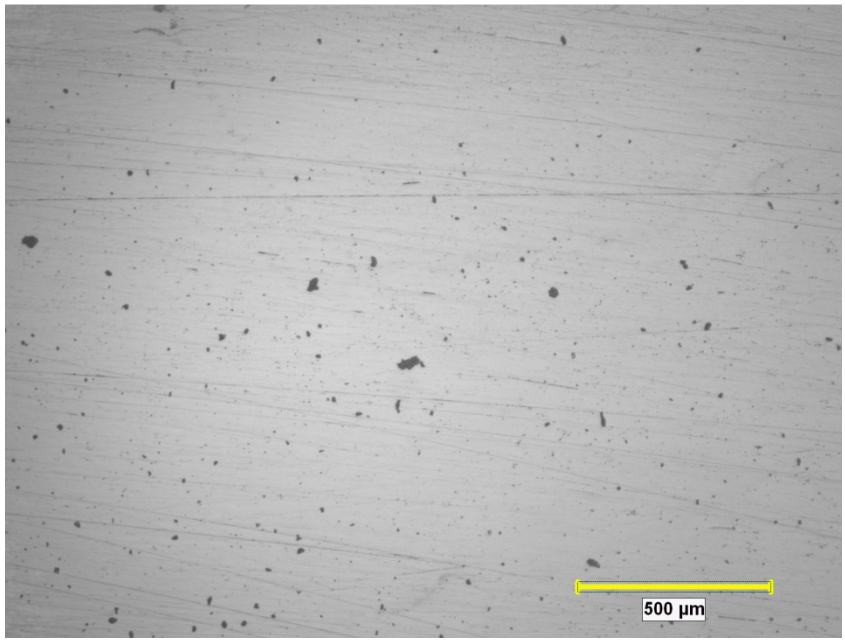

800 Grit

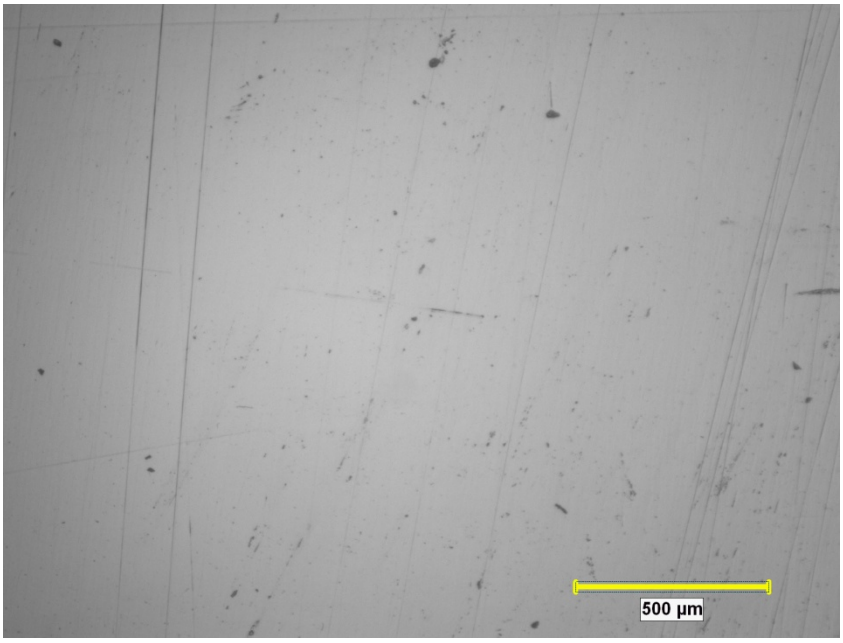

1200 Grit

APPENDIX 2:

Effect of drop size on contact angle (oil on steel 304)